Sustainable Chemistry and Pharmacy 46 (2025) 102070

Contents lists available at ScienceDirect

Sustainable Chemistry and Pharmacy

journal homepage: www.elsevier.com/locate/scp

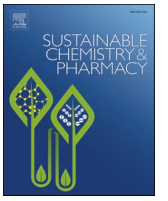

Geraniol:l-menthol eutectic mixtures; thermophysical properties and drug solubility

Mohammadreza Haftbaradaran Esfahani [a], Fernando Bergua [a,b], Ignacio Delso [c], Carlos Lafuente [a,b,*], Manuela Artal [a,b]

[a] Departamento de Química Física, Facultad de Ciencias, Universidad de Zaragoza, Zaragoza, Spain
[b] Instituto Agroalimentario de Aragón – IA2 (Universidad de Zaragoza – CITA), Zaragoza, Spain
[c] School of Pharmacy, University of East Anglia, Norwich, United Kingdom

ARTICLE INFO

Handling Editor: Borhane Mahjoub

Keywords:
Thermophysical properties
Geraniol
L-menthol
Eutectic solvents
Solubility active pharmaceutical ingredients

ABSTRACT

The study of eco-sustainable alternative solvents as the eutectic mixtures (ESs) is a fundamental pillar of the concept of green chemistry. Furthermore, the dissolution of pharmaceutical active ingredients (APIs) in ESs has shown to be a feasible strategy to improve the bioavailability of poorly soluble APIs in water. Here, three geraniol:l-menthol (GM) mixtures are characterized for the first time. The structure and thermophysical properties were evaluated and discussed. Furthermore, the ability of GM ES and pure geraniol (G) to dissolve five APIs was determined and compared with that of water and other ESs. No similar studies were found in the literature for this system. From NMR, a more slowly diffusion of the species as the l-menthol ratio increased was observed. All hydrodynamic radii were similar, about 6.8 Å. Also, no strong aggregation was observed. At 298.15 K, the values of density, free volume, and surface tension were about 890 kg/m^3, 72 %, and 28.5 mN/m, respectively. The dynamic viscosity ranged from 10 to 19 mPa s. These properties decreased as the G mole ratio increased. Furthermore, a parallel orientation of the adjacent dipoles was observed. Thermodynamic correlations and PC-SAFT equation of state were validated. The lowest solubility was obtained with water as solvent and the highest with pure G. Respectively, the values expressed as mole fraction of API were: $6.12{\cdot}10^{-6}$ and $2.31{\cdot}10^{-4}$ for nitrofurantoin, $4.17{\cdot}10^{-6}$ and $1.69{\cdot}10^{-3}$ for furosemide, $2.56{\cdot}10^{-8}$ and 0.028 for quercetin, $3.08{\cdot}10^{-5}$ and 0.026 for tetracycline, and $7.66{\cdot}10^{-7}$ and 0.042 for carvedilol.

1. Introduction

Over the last twenty years, green chemistry has emerged as a prevailing norm in response to growing apprehensions regarding environmental and human health (Becker et al., 2022). This approach prioritizes the creation of materials and chemicals that pose reduced risks, aiming to ensure the safety of both the ecosystem and individuals. Solvents represent a significant category of chemical substances that find extensive application across various industries. Despite their crucial role in industrial processes, solvents pose evident environmental risks due to their composition primarily derived from fossil fuels, as well as their flammable and toxic nature. As a result, extensive efforts have been made by researchers and scientists to explore and develop alternative sustainable agents and solvents that adhere to the principles of Green Chemistry (Zimmerman et al., 2020). Supercritical fluids, ionic liquids, and deep

* Corresponding author. Departamento de Química Física, Facultad de Ciencias, Universidad de Zaragoza, Zaragoza, Spain.
E-mail address: celadi@unizar.es (C. Lafuente).

https://doi.org/10.1016/j.scp.2025.102070
Received 8 April 2025; Received in revised form 2 June 2025; Accepted 4 June 2025
Available online 12 June 2025

eutectic solvents have been proposed as eco-friendly solvents. All of them have advantages and disadvantages and are more or less suitable depending on the application where they are to be implemented (Ma et al., 2025; Mushtaq et al., 2024; Quintana et al., 2022; Shaibuna et al., 2022). Fluids in the supercritical state are characterized by having properties of both gases and liquids: high diffusivity, density, and solvation capacity, and low viscosity. They stand out for the tunability of their properties, high mass transfer rates, and ease of recycling and removal. On the other hand, they have a limited polarity range and the necessary equipment is expensive. Among other properties, ionic liquids have excellent conductivity, negligible vapor pressure, and low flammability. Nevertheless, despite their reduced air pollution risk, their solubility in water poses environmental challenges. High costs and recycling difficulties hinder industrial adoption. Finally, deep eutectic solvents (DESs) have gained attention as cost-effective and environmentally friendly solvent media. In relation to its definition, a consensus has been achieved after some confusing beginnings (Oyoun et al., 2023). A DES is a mixture of two or more components whose melting temperature (T_m) is markedly lower than if it behaved ideally (T_m^{id}). That is, it exhibits a marked negative deviation from ideality. In addition, this deviation must be such that the system is liquid at the operating temperature in a composition range. Otherwise, the term eutectic solvent (ES) must be used. It is important to note that the eutectic point is not related to the formation of a complex, so a stoichiometric relationship is not necessary. Despite this, and following the initial articles, the composition of the mixtures studied in the literature are usually presented as molar ratio. The solid-liquid phase diagram depends on both the melting properties of the components, the entropic effect associated with the mixing process, and the interactions established between them. The interactions can be electrostatic, hydrogen-bond donor-acceptor, and van der Waals. The first ones are predominant when there are salts in the composition and the rest in mixtures of non-ionic compounds. Five types of eutectic systems have been described depending on the nature of the components. A quaternary ammonium salt mixed with an anhydrous or with a hydrated metal salt are DESs of type I and II. In type III, the quaternary ammonium salt is mixed with organic molecules as alcohols, acids, and amides. Eutectic mixtures of type IV containing a metal salt and small neutral organic compounds. Type V are combinations of the neutral organic substances. Types I to IV have hydrophilic character and the systems of type V are hydrophobics. Depending the affinity to water, the thermophysical properties of the eutectic mixtures are very different and the applications are complementary (Katrak et al., 2025; Li et al., 2025; Martín et al., 2024; Zheng et al., 2025). Other names are used in the literature to denote some eutectic systems. Thus, mixtures that include metabolites are known as natural deep eutectic solvents (NADESs) and belong basically to Types III and V. Systems that contain active pharmaceutical ingredients (APIs) are called therapeutical deep eutectic solvents (THEDESs) and are type V systems. Our group has focused its research on the characterization of both NADES and THEDES systems. Some examples are included in the references (Bergua et al., 2021a; Delso et al., 2019; Esfahani et al., 2024; Hernández-Serrano et al., 2023; López et al., 2020; Molero-Sangüesa et al., 2024; Padilla et al., 2024).

In pharmacology, NADESs have different applications. They are used in the extraction of bioactive compounds, as solubilizing and stabilizing agents for drugs, functional additives, reaction media, or catalysts in biosynthesis. Furthermore, THEDESs can be considered as the liquid form of one or more drugs (Ganorkar et al., 2025; Ma et al., 2025). The study of DESs has made much more progress in the search for new systems for specific applications than in understanding their structure and thermodynamic behavior. Expanding our knowledge of these aspects will allow us to improve the customized design of sustainable solvents that would optimize processes. Continuously developing computational tools, such as PARIS III developed by the Environmental Protection Agency, provide the best alternative solvent based on the values of a wide variety of thermophysical properties (Harten et al., 2020). In this article, we analyze the three aspects (structure, thermophysical properties, and solvent capacity) of the geraniol:l-menthol system. This is a type V ES that has not been previously evaluated in the literature. Geraniol ((E) 3,7-dimethyl-2,6-octadien-1-ol) is an acyclic monoterpene alcohol that is found in essential oils like Monarda fistulosa, Ninde oil, Rose oil, Palmarosa oil, and Citronella oil. It has been studied for its insect repellent, antimicrobial, and solvent properties (Chen and Viljoen, 2010; Maczka et al., 2020). Menthol (1R, 2S,5R)-2-isopropyl-5-methylcyclohexane), a cyclic monoterpenoid alcohol, can be obtained through chemical synthesis or extracted from plants in the menthe family. The l-menthol (M) is the most abundant isomer in the nature. It has various therapeutic effects such as analgesic, antitussive, antiviral, and anticancer activities (de Castro Teixeira et al., 2024; Zielińska-Błajet et al., 2021). Both compounds have been recognized as safe by the European Food Safety Authority (EFSA) ("Conclusion on the peer review of the pesticide risk assessment of the active substance geraniol," 2012; "Safety and efficacy of secondary alicyclic saturated and unsaturated alcohols, ketones, ketals and esters with ketals containing alicyclic alcohols or ketones and esters containing secondary alicyclic alcohols from chemical group 8 when used as flavourings for all animal species," 2016). Their eutectic mixtures, as well as combinations of other terpenes and terpenoids, have potential as cost-effective and environmentally friendly solvents in NADESs formulation. Among its applications, we highlight its use as a vehicle for drugs that are poorly soluble in aqueous solution. A marked increase in bioavailability has been observed when they are dissolved in ESs (Abdelquader et al., 2023; Ganorkar et al., 2025). The field of pharmaceutical sciences encounters significant obstacles related to the solubility in water and permeability of drugs, leading to suboptimal pharmacokinetics and limited bioavailability of APIs. It is important to note that approximately 40 % of APIs with market approval and the most under development exhibit poor solubility in aqueous media. In addition, options to formulate oral liquid medications are limited for APIs classified as Class II and IV drugs according to the Biopharmaceutical Classification System (BCS), but highly recommended for older patients, infants, and patients with swallowing problems. These issues also extend to nutraceuticals, where natural antioxidants and phytochemicals often suffer from biological instability and low solubility, stability, bioavailability, and specificity. Various strategies have been suggested to overcome these problems including physical modifications (reducing particle size, modifying crystalline form, and solid dispersions), and chemical modifications (pH adjustment, buffer use, derivatization, complexation, and salt formation). Additionally, various methods can be used, including the use of adjuvants as surfactants, solubilizers, and new excipients. A desirable solvent for pharmaceutical applications must be able to maintain the efficacy of APIs while also meeting the necessary criteria for human patient administration. If the solvent is also composed by bioactive compounds, as is the

Table 1
Compounds used in this work.

Chemical (acronym)	CAS Nº	Supplier	Purity[a]	M_i/ g·mol^{-1}	T_m/ K
Geraniol (G)	106-24-1	Sigma-Aldrich	>98.7	154.25	183[b]
L-menthol (M)	2216-51-5	Sigma-Aldrich	>99	156.27	315.2[c]
Nitrofurantoin (NF)	67-20-9	Sigma-Aldrich	>98	238.16	536[d]
Furosemide (F)	54 -31-9	Acofarma	99.2	330.75	482 [d]
Quercetin (Q)	117-39-5	Sigma-Aldrich	>95	302.23	589.65 [d]
Tetracycline (TC)	60-54-8	Sigma-Aldrich	>95	444.43	445.6 [d]
Carvedilol (CVD)	72956-09-3	Acofarma	99.8	406.5	387.65 [d]
Tetramethylsilane (TMS)	75-76-3	Fisher	99.9	88.22	174.09 [d]

[a] as stated by the supplier (wt. %).
[b] Ref. (Štejfa et al., 2015).
[c] Ref. (Bergua et al., 2022b).
[d] Ref. ("PubChem Database," n.d.)

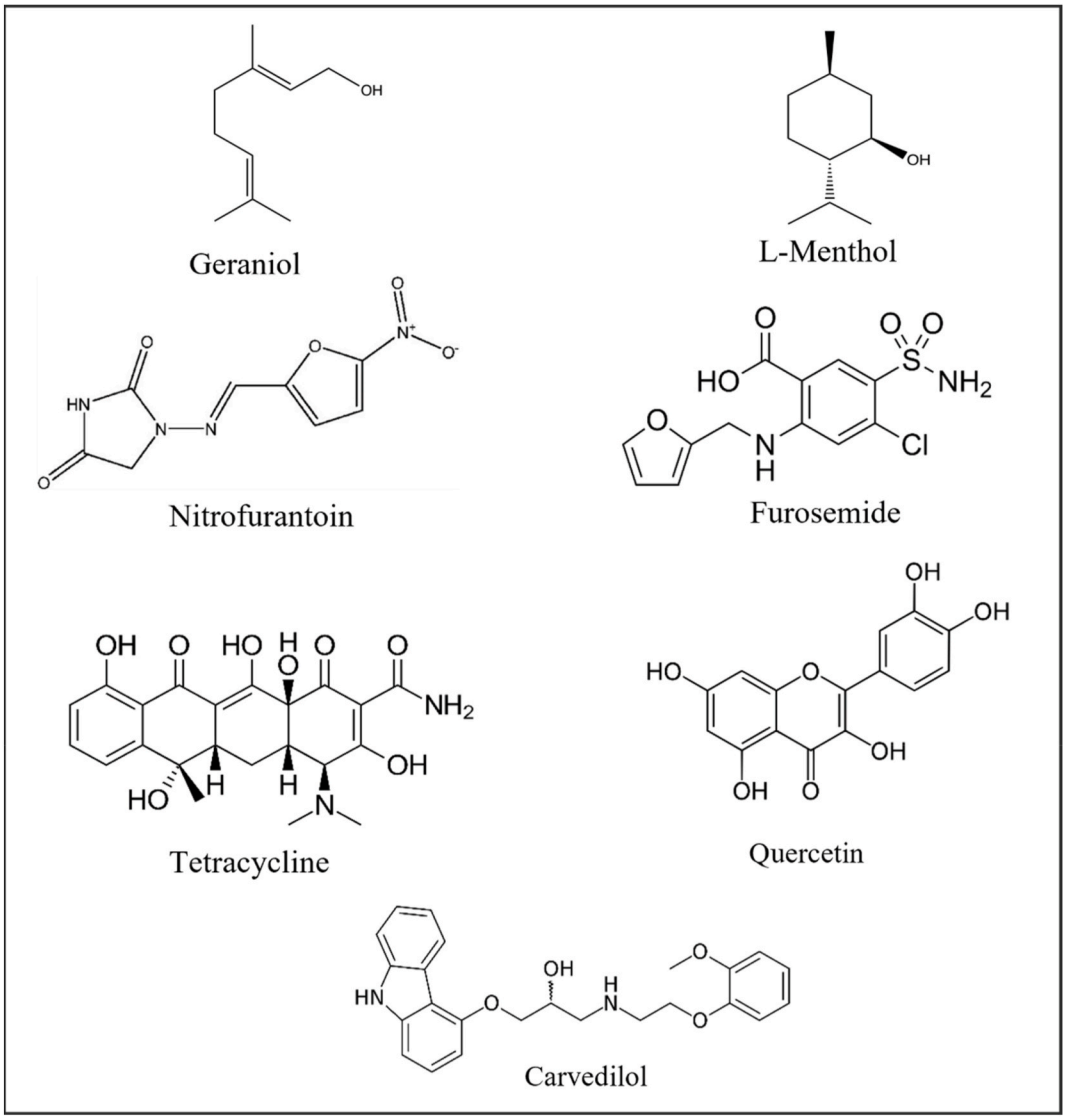

Fig. 1. Structure of the compounds investigated in the study.

Table 2
Characteristics of the studied geraniol:l-menthol eutectic solvents (GM ESs).

Acronym	Component 1	Component 2	Molar ratio	M^a/ (g/mol)
GM12	Geraniol	L-menthol	1:2	155.60
GM11	Geraniol	L-menthol	1:1	155.26
GM21	Geraniol	L-menthol	2:1	154.90

case with many NADESs, the health benefits of the final formulation are enhanced. In this context, it is essential to understand the structure and interactions within the solvent used, as well as its thermophysical behavior. However, the number of studies including characterization and application is very limited.

In the present investigation, the structure and interactions between the compounds of the binary system, geraniol and L-menthol, were evaluated by nuclear magnetic resonance spectroscopy (NMR) techniques. Moreover, different thermophysical properties of three compositions were measured and discussed. They were the phase change properties, density, speed of sound, refraction index, isobaric molar heat capacity, static permittivity, surface tension, and viscosity. The working pressure was 0.1 MPa and the temperature ranged from 278.15 to 338.15 K. The measured data were modeled and correlated with several equations. Finally, the solubility of nitrofurantoin, furosemide, quercetin, tetracycline, and carvedilol in pure geraniol, and in the studied binary mixtures was determined.

2. Materials and methods

2.1. Materials

The chemicals used to prepare the three eutectic mixtures characterized were geraniol (G) and L-menthol (M). Also, the solubility of five active pharmaceutical ingredients (APIs) was evaluated. They were nitrofurantoin (NF), furosemide (F), quercetin (Q), tetracycline (TC), and carvedilol (CVD). Tetramethylsilane (TMS) was used as reference fluid in the RMN experiments. All substances were used as received without any further treatment. The characteristics and structures of each compound are reported in Table 1 and Fig. 1.

2.2. Preparation of ESs

The preparation process began with the weighing of the pure compounds in the appropriate proportions using a PB210S Sartorius balance with an uncertainty of 10^{-4} g. Later, the flask was simultaneously stirred and heated at 323.15 K until a homogeneous liquid phase was obtained. The samples were slowly cooled and kept in the dark at 298 K until use. The water content in the mixtures was determined by triplicate by the Karl-Fischer method (automatic titrator Crison KF 1S–2B) and was lower than 300 ppm in all cases. The presence of water in the samples of both pure compounds and mixtures was undetectable with NMR technique. Table 2 lists the characteristics of the ESs studied: the acronyms used through the manuscript, components, molar ratio, and molar mass (M_{ES}) of each mixture. The M_{ES} was calculated from the mole fraction (x_i) and molar mass (M_i) of each component.

$$M_{ES} = \Sigma_i M_i x_i,$$

2.3. Nuclear magnetic resonance

NMR experiments were acquired using a Bruker NEO spectrometer operating at 500 MHz and equipped with a 5 mm iProbe. All the experiments were recorded at 298K. Chemical shifts were referenced to tetramethylsilane (TMS) as either internal or external reference, showing a chemical shift both in ^{1}H and ^{13}C of 0.0 ppm. Quantitative ^{1}H NMR spectra were recorded with a one-pulse sequence with 30° flip angle (Bruker pulse program *zg30*) with a spectral width of 16 ppm centred at 5 ppm, 16 scans for each spectrum and a recovery time of 15 s, for quantitative analysis no TMS was added and measured from the same batch of the corresponding ES that used for the thermophysical measurements. ^{13}C NMR spectra were obtained using an ATP sequence (Bruker pulse program *jmod*), with a spectral width of 240 ppm centred at 100 ppm and 64 scans for each spectrum. All ^{1}H and ^{13}C signals were unambiguously assigned using conventional 1D and 2D experiments (APT, DQF-COSY, ^{1}H–^{13}C HSQC, and ^{1}H–^{13}C HMBC). Diffusion experiments were acquired using a stimulated echo experiment with bipolar gradients (Bruker pulse program *stebpgp1s*). The spectral width was set to 15 ppm centred at 5 ppm, acquiring 8 scans per increment, and a relaxation delay of 2 s. Big delta was set to 160 ms and 12 ms for small delta. Gradient pulses amplitude varied through 64 steps from 2 % to 98 %, with a calibrated maximum gradient strength of 5.35 G/cmA. The self-diffusion coefficients, D, were calculated by fitting the intensity of each signal to the following function:

$$I(g) = I_{G=0} \exp\left[-D\gamma_H^2 G^2 \delta^2 \left(\Delta - \frac{\delta}{3} - \frac{\tau}{2} \right) \right] \quad \text{(eq. 1)}$$

Where $I(g)$ is the measured intensity; $I_{G=0}$ is the intensity in the absence of gradient; D is the self-diffusion coefficient; γ_H is the gyromagnetic constant of ^{1}H nucleus; G is the strength gradient; δ is the duration of the bipolar gradient; Δ is the diffusion time and τ is the time between the end of the gradient and the beginning of the next pulse. To assess the uncertainty and error in the determination

Table 3
Overview of the different apparatus utilized for measurement of thermophysical properties.

Property	Devices	$u(T)$/K	$U_c(Y)^a$	$MRD(Y)^b$/%
Density, ρ	Oscillating U-tube density meter, Anton Paar DSA 5000−[c]	0.01	0.05 kg m^{-3}	0.004
Speed of sound, u	Sing-around technique in a fixed-path interferometer, Anton Paar DSA 5000−[c]	0.01	0.5 m s^{-1}	0.026
Isobaric molar heat capacity, $C_{p,m}$	Differential scanning calorimeter, TA Instruments DSC Q2000−[d]	0.5	1 %	0.028
Refractive index, n_D	Standard Abbe refractometer, Abbemat-HP refractometer Dr. Kernchen−[e]	0.01	$2{\cdot}10^{-5}$	0.007
Static permittivity, ε_r	Capacitance and resistivity method, Agilent 4263BA LCR high precision impedances analyzer 2 MHZ	0.01	0.02	0.11
Surface tension, γ	Drop volume tensiometer, Lauda TVT-2−[e,f]	0.01	1 %	0.21
Kinematic viscosity, ν	Capillary viscosimeter Ubbelohde, Schoot-Geräte AVS-440	0.01	1 %	0.28

[a] $k = 2$ (0.95 level of confidence); [b] $MRD(Y) = \frac{100}{n}\sum_{i=1}^{n}\left|\frac{Y_{i,lit} - Y_{i,exp}}{Y_{i,exp}}\right|$

of self-diffusion coefficient, two more mixtures from the same compositions (GM11, GM12, and GM21) were separately and freshly prepared, therefore three replicas for each system were performed. 2D-NOESY experiments were performed using the Bruker pulse program *noesygpphpp* with a spectral width of 12 ppm centred at 5 ppm, acquiring 256 increments and 4 scans per increment, and a recovery delay of 2 s. Increasing values of mixing time were used: 300, 600, 900, and 1200 ms. 2D-ROESY experiments were performed using the Bruker pulse program *roesyphpp.2* with the same parameters as in 2D-NOESY experiments and using a spinlock time of 200 ms. For all the above-mentioned experiments, the ^{1}H 90° pulse was calibrated for each sample, using in all cases an optimized pulse length of 7 μs and a power of 16.7 W, while the pulse length and power employed for ^{13}C was 14 μs and 85.1 W respectively.

2.4. Phase change

A differential scanning calorimeter (TA Instruments DSC Q2000) was used to determine the temperatures and enthalpies of the phase change of our mixtures. This device includes an RCS cooling system. The calibrations of the temperature and heat flow were performed with a standard of Indium. The uncertainties in T_m and $\Delta_m H$ were estimated from the differences between the expected values of the standard and those from the calibration. The values were 0.5 K and 1 kJ/mol, respectively. For each sample, an amount from 5 to 10 mg of mixture was weighed and introduced into an aluminum pan. Afterward, it was firstly cooled at 203–213 K at 3 K/min and later heated at the same scanning rate up to 10 above the phase change. The reported temperatures correspond to the maximum peak because of the asymmetric peak shapes.

2.5. Thermophysical properties

Six thermodynamic properties and one transport property were measured with different thermostatically controlled apparatus. These methods have been frequently documented in the literature so we provide only essential information in this paper. The vibrating tube densimeter and sound analyzer was calibrated with two reference fluids: air and water MilliQ (resistivity of 18.2 μS·cm^{-1}). The latter fluid was also used to calibrate both the refractometer and tensiometer. Each surface tension value of each replica was given as the average of 16 drops. In the DSC calorimeter, the zero-heat flow procedure with a sample of synthetic sapphire was used as standard reference. or all properties, each tabulated value was calculated as the average of two replicates in which the coefficient of variation was lower than the experimental uncertainty. Table 3 provides a summary of the type, standard uncertainty in temperature $(u(T))$, and calculated combined expanded uncertainties $(U_c(Y))$ for each property of each device. Additionally, they were checked with benzene as standard fluid (Antón et al., 2017). The mean relative deviations (MRD(Y)) in comparison with the literature data are found in Table 3.

2.6. Solubility study

There are various techniques for determining thermodynamic or equilibrium solubility. We used a modified shake-flask method (Baka, 2010) to determine the solubility of nitrofurantoin, furosemide, quercetin, tetracycline, and carvedilol in the ESs studied. Despite its drawbacks, it is considered one of the most reliable methods. It is used to validate new procedures that are less laborious and faster (Hokkala et al., 2024; Könczöl and Dargó, 2018). This technique involves the addition of solute to the solvent until it reaches supersaturation, followed by the analysis of the dissolved portion. A Selecta Ultrasons-H ultrasonic bath with 15-min cycles (from 30 to 150 min) at 60 Hz was used to ensure proper mixing. A water recirculation system at 298.15K with a Julabo MC bath ($u(T) = 0.01$ K) prevented the increase in temperature due to the ultrasonic waves (Mulet et al., 2016). After settling, each sample of a solubility experiment was subjected to centrifugation for 5 min and 15000 rpm (Nahita Model 2716) and filtration using a PES syringe filter with a pore size of 0.22 μm. Afterward, two aliquots were removed and analyzed by UV-VIS using a VWR 6300 PC spectrophotometer with

an uncertainty of 0.2 nm. A wavelength scan was conducted within the range of 500 to 200 nm and the maximum absorbance was taken. Each analysis was repeated three times and each solubility experiment was replicated four times. From them, a value of average absorbance was calculated and compared with the corresponding calibration curve for each API (Table S1). The Q-test and Grubbs tests were performed using the QI Macros 2025 Excel add-in, and t-tests were conducted with the standard Excel Data Analysis Toolpak. The calculated Q values were consistently below the critical Q thresholds, supporting the reliability of the data for all three APIs.

3. Theory and calculations

3.1. PC-SAFT EoS

A comprehensive description of this equation of state can be found in the literature (Gross and Sadowski, 2001, 2002). Here, we will give a brief summary. The Helmholtz energy ($\tilde{a}$) is described as the sum of an ideal gas contribution ($\tilde{a}^{id}$) and a residual one ($\tilde{a}^{res}$). The last one contains a repulsive term used by the hard-chain reference system ($\tilde{a}^{hc}$), and various attractive contributions as the dispersive ($\tilde{a}^{dis}$) and association ($\tilde{a}^{assoc}$) terms. The equations are:

$$\tilde{a}^{res} = \tilde{a}^{hc} + \tilde{a}^{dis} + \tilde{a}^{assoc} \quad \text{(eq. 2)}$$

$$\tilde{a}^{hc} = m\tilde{a}^{hs} - (m-1)\ln g^{hs} \quad \text{(eq. 3)}$$

$$\tilde{a}^{dis} = -2\pi\rho m^2\left(\frac{\varepsilon}{kT}\right)\sigma^3\sum_{i=0}^{6}\left[a_{0i}+\frac{m-1}{m}a_{1i}+\frac{m-1}{m}\frac{m-2}{m}a_{2i}\right]\eta^i - \pi\rho mkT\left(\frac{\partial\rho}{\partial p}\right)_{hc} m^2\left(\frac{\varepsilon}{kT}\right)^2\sigma^3\sum_{i=0}^{6}\left[b_{0i}+\frac{m-1}{m}b_{1i}+\frac{m-1}{m}\frac{m-2}{m}b_{2i}\right]\eta^i \quad \text{(eq. 4)}$$

$$\tilde{a}^{assoc} = \sum_A\left[\ln\left(1+\rho X^A\Delta\right)^{-1} - \frac{\left(1+\rho X^A\Delta\right)^{-1}}{2}\right] + \frac{1}{2}S \quad \text{(eq. 5)}$$

$$\Delta = \kappa^{A_iB_i}\sigma^3 g^{hs}\left[\exp\left(\frac{\varepsilon^{A_iB_i}}{kT}\right)-1\right] \quad \text{(eq. 6)}$$

where m is the chain segment number, g^{hs} is the radial pair distribution function of the segments, $\tilde{a}^{hs}$ is the Helmholtz energy of the hard sphere, ρ is the density, p is the pressure, T is the temperature, σ is the segment diameter, ε is the segment energy, η is the packing fraction, X^A is the fraction of unbonded monomers, Δ is the tendency to form n-mers, $\kappa^{A_iB_i}$ is the association volume, $\varepsilon^{A_iB_i}$ is the association energy, and S is the number of associated sites of the compound. The thermodynamic properties of n-alkanes were used to obtain the values of the *universal constants* ($a_{0i},\ a_{1i}, a_{2i},\ b_{0i}, b_{1i},$ and b_{2i}). From all this, five parameters and an association scheme are needed to characterize each pure substance. Three of them are geometric parameters (m, σ and ε) and two are association parameters ($\kappa^{A_iB_i}$ and $\varepsilon^{A_iB_i}$). For our compounds, the values were taken from the literature (Esfahani et al., 2024; Martins et al., 2018) and are listed in Table S2. For modeling mixtures, several mixing rules can be used. We have chosen the following:

$$\sigma_{ij} = \left(\sigma_i + \sigma_j\right)/2 \quad \text{(eq. 7)}$$

$$\varepsilon_{ij} = \sqrt{\varepsilon_i\varepsilon_j}\left(1-k_{ij}\right) \quad \text{(eq. 8)}$$

$$\kappa^{A_iB_j} = \sqrt{\kappa^{A_iB_i}\,\kappa^{A_jB_j}} \quad \text{(eq. 9)}$$

$$\varepsilon^{A_iB_j} = \left(\varepsilon^{A_iB_i} + \varepsilon^{A_jB_j}\right)/2 \quad \text{(eq. 10)}$$

where the subscripts i and j refer to each of the compounds present in the mixture, and k_{ij} is the binary interaction parameter.

3.2. Estimation of the isobaric molar heat capacity

The correlation of Taherzadeh et al. (2020) allow to estimate the $C_{p,m}$ of mixtures as follows:

$$C_{p,m} = A + 132.27\ T^{1/4}, \quad \text{(eq. 11)}$$

$$A = 3.8\cdot10^{-4}\frac{M^3}{p_c^6} + 6.3\cdot10^{-5}M_{ES}^{2\omega} - \frac{24577.4}{M_{ES}} - 94.9, \quad \text{(eq. 12)}$$

Where T is the temperature and M_{ES} is the molar mass of the ES. The critical pressure (p_c) and the acentric factor (ω) of each mixture

were estimated from the Lee-Kesler (LK) mixing rules (Lee and Kesler, 1975):

$$p_c(\text{bar}) = (0.2905 - 0.0850\omega)\frac{83.1447T_c}{V_c}, \quad \text{(eq. 13)}$$

$$\omega = \sum_{n=1}^{3} x_n\omega_n, \quad \text{(eq. 14)}$$

$$V_c(\text{mL / mol}) = \sum_{n=1}^{3}\sum_{m=1}^{3} x_n x_m V_{c,mn}, \quad \text{(eq. 15)}$$

$$T_c(\text{K}) = \frac{1}{V_c^{0.25}}\sum_{n=1}^{3}\sum_{m=1}^{3} x_n x_m V_{c,mn}^{0.25} T_{c,mn}, \quad \text{(eq. 16)}$$

$$V_{c,mn}(\text{mL / mol}) = \frac{1}{8}\left(V_{c,n}^{1/3} + V_{c,m}^{1/3}\right)^3, \quad \text{(eq. 17)}$$

$$T_{c,mn}(\text{K}) = \left(T_{c,n}T_{c,m}\right)^{0.5}, \quad \text{(eq. 18)}$$

Where the subscripts n and m represent each component, and mn is the subscript indicating binary interaction term. T_c and V_c are the critical temperature and critical volume of the ES.

3.3. Estimation of the critical temperature

Both PC-SAFT EoS and the LK mixing rules provide values of T_c of the mixtures (eqs. (2)–(18)). They can also be calculated using the equations of Guggenheim (Guggenheim, 1945) and Eötvos (Shereshefsky, 1930):

$$\gamma = \gamma_0(1 - T/T_c)^{11/9}, \quad \text{(eq. 19)}$$

$$\gamma(M_{ES}/\rho)^{2/3} = K(T_c - T), \quad \text{(eq. 20)}$$

Where γ_0 is the surface tension at 0 K, M_{ES} is the molar mass of the ES, and γ and ρ are the surface tension and density at the temperature T.

3.4. Estimation of the surface tension

The γ can be correlated to both the n_D and η. For the first, we used the equation of Papazian (1971) and for the second, those of Pelofsky and Murkerjee (Pelofsky, 1966):

$$\gamma = A\left(\frac{n_D^2 - 1}{2n_D^2 + 1}\right) + B, \quad \text{(eq. 21)}$$

$$\ln\gamma = \ln A_1 + \frac{B_1}{\eta}, \quad \text{(eq. 22)}$$

$$\ln\gamma = \ln A_2 + \frac{B_2}{3}\ln\eta, \quad \text{(eq. 23)}$$

Where $A, B,\ A_1, A_2$, B_1, and B_2 are the fit coefficients.

4. Results and discussion

4.1. NMR studies

For this work, we used NMR as a technique for determine with precision the exact composition of the three ES prepared, to obtain insights into the preferential molecular interactions formed among the components in the mixture, and to determine de self-diffusion coefficients for each component in the different mixtures. The addition of a small amount of tetramethylsilane (TMS) to the ESs as inert reference has allowed us to compare the degree of aggregation and strength of the intermolecular interactions between the components. Finally, we determined the sensitivity of self-diffusion coefficient to small variation in the ES composition by preparing three replicas and assessing the error.

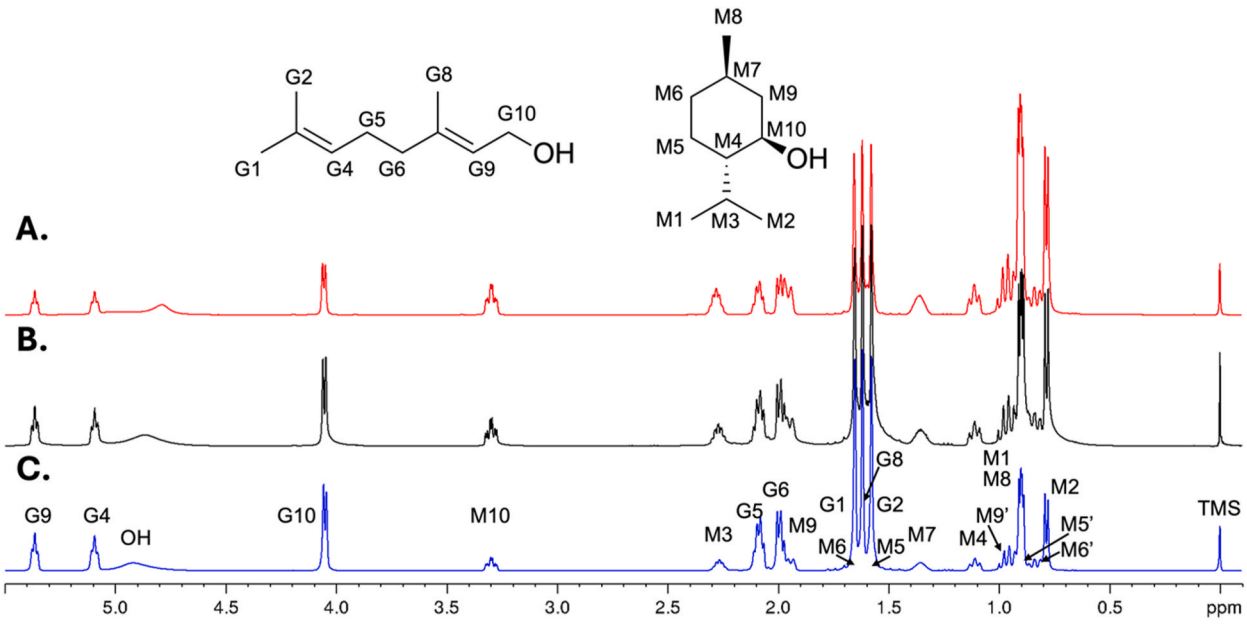

Fig. 2. ^{1}H NMR spectra of the mixtures studied. **A.** (—), geraniol:l-menthol (2:1) (GM21), **B.** (−), geraniol:l-menthol (1:1) (GM11), and **C.** (—), geraniol:l-menthol (1:2) (GM12).

4.1.1. *Effect of the composition in the ^{1}H NMR and ^{13}C NMR signals*

The absence of significative changes in the chemical shifts and the presence of all resonances for both components in ^{1}H and ^{13}C NMR spectra (Fig. 2, S1, and S2) indicated neither a chemical reaction among components nor the formation of any new species. This fact was confirmed by comparison between the spectra of the dilution in DMSO-d_6 and $CDCl_3$, and those of the pure species (Fig. S3). The composition of each ES prepared was calculated from the ^{1}H NMR spectra integrating exclusively signals arising from one of the species. The molar ratio of G and M in the mixtures was (1:2.06) for GM12, (1:1.06) for GM11, and (2:1.09) for GM21, with an uncertainty of $u(x) = 0.068$. Variations of chemical shift throughout the composition respond to changes in the chemical environment.

In the ESs studied, no significant changes were observed in the ^{1}H NMR spectrum (<0.05 ppm) in any signal, across the 3 GM ES, suggesting a limited perturbation in the local environment. Analogously, mobile protons from the hydroxyl groups showed very limited change, under a unique broad signal, indicating medium-rate chemical exchange. Similar behaviour was observed across compositions in the ^{13}C NMR spectra, with variations below the threshold of 0.1 ppm. Only carbon 3 in M showed an upfield shifting as its proportion increases (Fig. S4). Considering the proximity of this carbon to the hydroxyl group, the shift could indicate the greater proportion of M engaging in hydrogen bonds in mixtures richer in this terpene.

4.1.2. *NOESY and ROESY experiments*

NOESY and ROESY experiments rely on the detection of the nuclear Overhauser effect (nOe) arising from the perturbation due to the spatial proximity of nuclei with inverted spin population. Therefore, nOe-based experiments can provide structural information about the preferential molecular dispositions, and consequently about the intermolecular interactions. The presence of cross-peaks in the NOESY spectra correlating two different nuclei indicate spatial proximity, typically accepted within the range of 5 Å. The cross-peak sign correlates with the rate of molecular tumbling, being positive for species in the fast movement regime, and negative for slow tumbling molecules, either large molecules and supramolecular structures or in highly viscous solvents. In the NOESY spectra for all three compositions (Fig. 3), it can be observed the presence of cross-peaks arising from intramolecular contacts (See Figs. S5–S7 for other mixing times and Fig. S8 for the pure components). The NOESY spectrum for the most viscous sample (GM12) showed several cross-peaks between G and M due to intermolecular contacts, and between distant protons in the same compound. Besides, many cross-peaks of negative sign appeared while only the most intense intramolecular contacts remain as positive signals. This phenomenon could be due to the additive effects of increased viscosity, greater size and strength of aggregates, and a more efficient spin-spin relaxation in slow molecular tumbling regime. Among the most relevant contacts (cross-peaks correlating nuclei at less than 5 Å), we stand out the interactions between methyl groups 1 and 2 with hydrogens 9 and 10 of neighbouring G molecules, as well as those between hydrogens 9 and 10 of G with those 1, 2, and 10 of M, and methyl groups 1 and 2 of G with 3 and 4 of M. All this suggested an important contribution of dispersion forces in the intermolecular interaction (Fig. 4A). It is worth noting the absence of cross-peaks due to intercomponent correlations between hydrogens and hydroxyls, which would demonstrate the presence of hydrogen bonds. This could suggest the low abundance or duration of this type of interactions in this system. Highlighted are intramolecular correlations of hydrogens 1 and 2 with 4 and 9 in geraniol (G1, G2 with G4, G9) in orange, and intermolecular correlations of hydrogens G1, G2 with M3 and M10 shown in green, and G4, G10 with M1, M2 in purple. Dotted black circles indicate areas where correlation M10 and G10 would appear. Finally, ROESY experiments were acquired to confirm the intermolecular cross-peaks observed in the NOESY spectra are

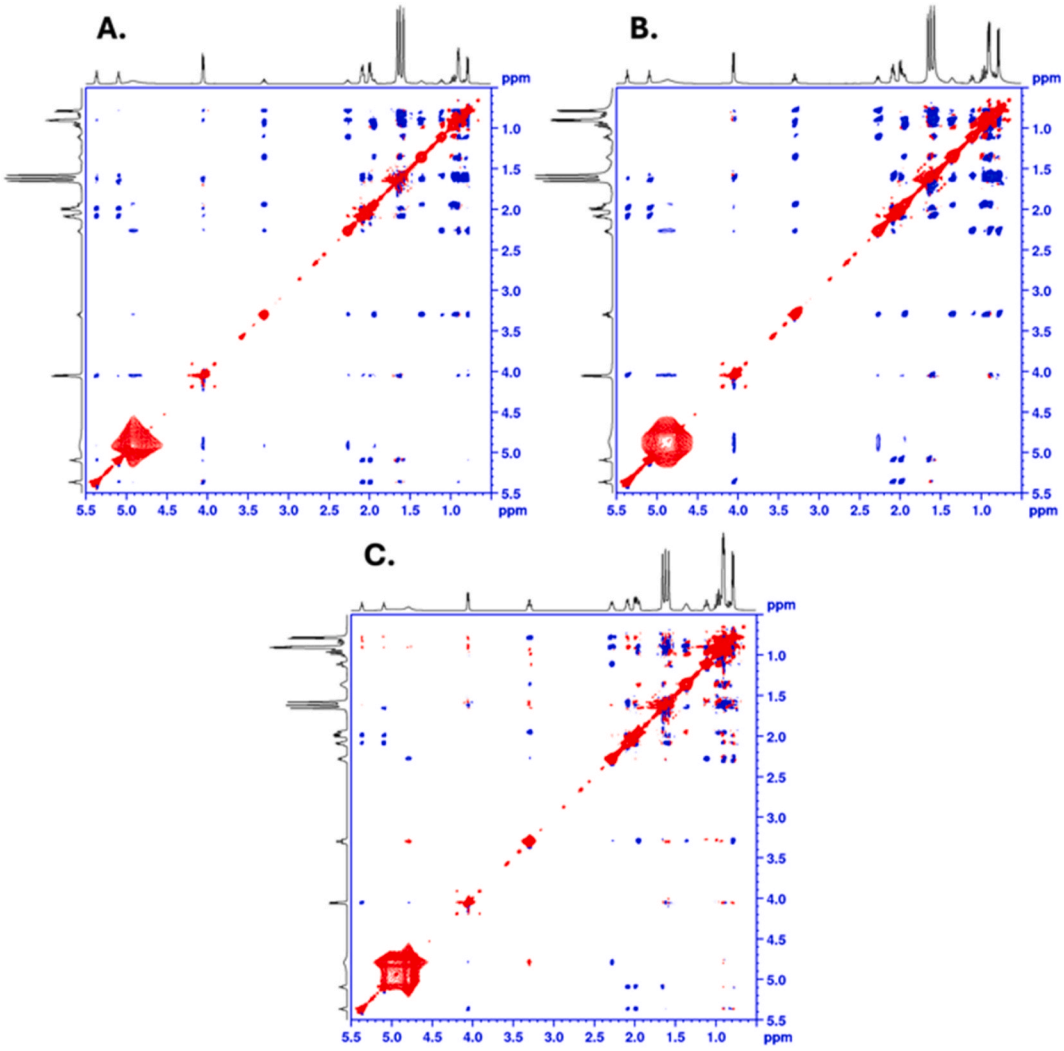

Fig. 3. NOESY spectra acquired with a mixing time of 600 ms for the mixtures studied. **A.** geraniol:l-menthol (2:1) (GM21), **B.** geraniol:l-menthol (1:1) (GM11), and **C.** geraniol:l-menthol (1:2) (GM12). Spectra have been symmetrised to reduce the intense T1 noise arising from sharp signals from methyl groups.

arising from legitimate intermolecular contacts and they are not spin diffusion artifacts induced by the high ES viscosity. Here, the presence of negative cross-peaks (as opposed to positive diagonal) is due exclusively the close proximity of two nuclei (or at least one nucleus from each spin systems), and not to the spin diffusion. As shown in Fig. 4B for the most viscous mixture, the abundance of cross-peaks both inter- and intramolecular cross-peaks demonstrated the authenticity of NOESY cross-peaks.

4.1.3. Determination of apparent molecular size using diffusion NMR experiments

Diffusion experiments are based in pulsed field gradients (PFG-NMR) and rely on the molecular Brownian motion in the three dimensions, being the diffusion on the vertical axis the one detected in this experiment. This experiment is frequently used to investigate the formation of aggregates and to evaluate the strength of intermolecular interactions in eutectic mixtures (Sil et al., 2023). However, this is the main reason why the diffusion of DES components frequently does not follow the Stokes-Einstein equation (eq (24)), and why the comparison of diffusion coefficients across different mixtures is not reliable.

$$D = \frac{k_B T}{6\pi\eta r_{H,app}}, \qquad \text{(eq. 24)}$$

where D is the diffusion coefficient, k_B is the Boltzmann constant, T is the temperature, η is the dynamic viscosity, and $r_{H,app}$ is the apparent hydrodynamic radius. In this work, we introduce the application of TMS as a useful reference that makes possible comparing diffusion data among different mixtures. This compound has no dipole moment, spherical structure, very low chemical reactivity, and it does not show any interaction with any of the mixture components, meaning that its hydrodynamic radius will not change due to the

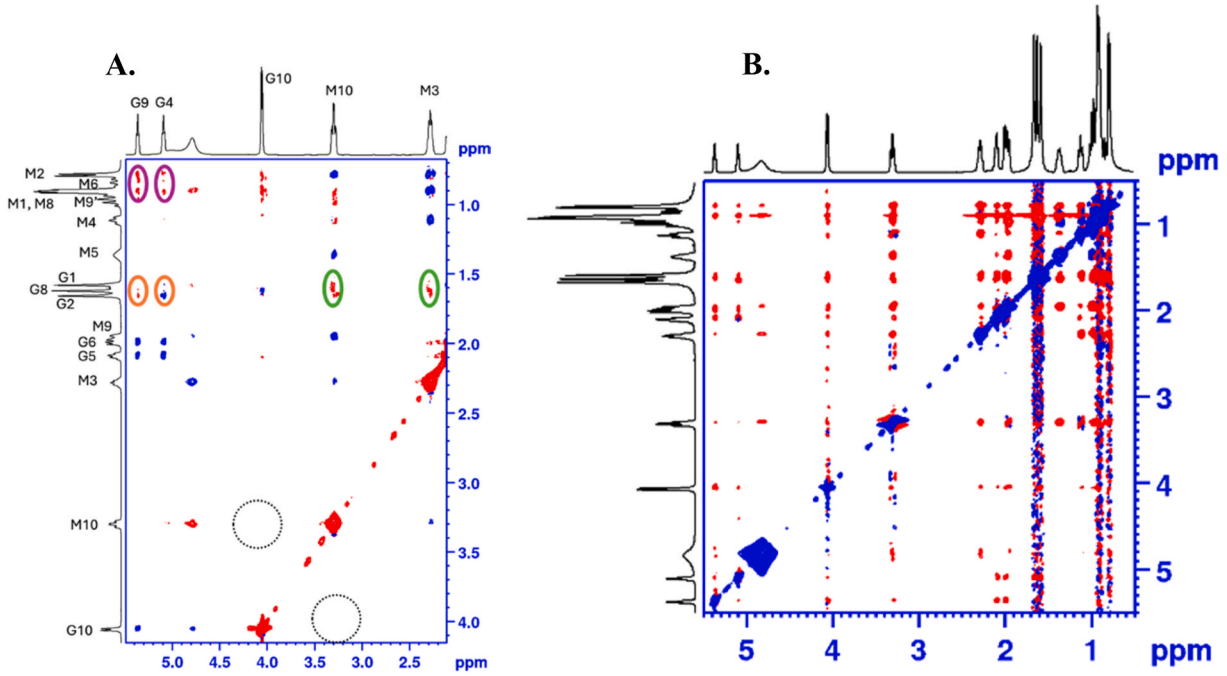

Fig. 4. **A.** NOESY spectrum for the mixture geraniol:l-menthol (1:2) (GM12). **B.** ROESY spectrum of ES geraniol:l-menthol (1:2) (GM12) with a spin-lock period of 200 ms.

Table 4
Averaged self-diffusion coefficients (D) and apparent hydrodynamic radii ($r_{H,app}$) at 298 K of each component in the GM ESs, for pure G, and diluted in deuterated solvent (DOSY representations are in Fig. S9).

	10^{11} D(G)/m^2/s	10^{11} D(M)/m^2/s	10^{11} D(TMS)/m^2/s	$r_{H,app}$ (G)/ Å	$r_{H,app}$ (M)/ Å
GM21	10.12	10.08	27.24	6.73	6.75
GM11	7.82	7.77	21.24	6.79	6.84
GM12	5.77	5.72	15.89	6.88	6.94
GM11 diluted in $CDCl_3$	180.57	192.57	253.20	3.51	3.28
GM11 diluted in DMSO-d_6	32.56	32.44	52.29	4.05	4.03
Pure G	17.03		44.13	6.48	
Pure G diluted in DMSO-d_6	32.03		51.79	4.04	
Pure M diluted in DMSO-d_6		34.84	56.26		4.04

surrounding medium (Cabrita and Berger, 2001). Therefore, referencing the measured diffusion coefficients to the one of TMS removes the dependance to temperature and viscosity, enabling the comparison of apparent molecular size among different compositions and proportions. Under this assumption, the ratio of diffusion coefficients will be inversely proportional to the ratio of $r_{H,app}$,

$$\frac{D(\mathrm{TMS})}{D(i)} = \frac{r_{H,app}\ (i)}{r_H(\mathrm{TMS})}, \qquad \text{(eq. 25)}$$

where the hydrodynamic radius of TMS is considered a constant with an average value of 2.5 Å (Virk et al., 2016). Therefore, for every sample containing TMS it can be calculated the apparent hydrodynamic radius of any other species using the following equation:

$$r_{H,app}\ (i) = \frac{D(\mathrm{TMS})}{D(i)} \cdot 2.5, \qquad \text{(eq. 26)}$$

Table 4 shows the values of D measured for G, M, and TMS in each mixture. Diffusion coefficients for the three species decreased in mixtures rich in M, due to the increase in viscosity, and showed similar values for G and M across proportions and in the diluted solutions. While the absolute value of D cannot be compared across samples, calculated $r_{H,app}$ for both G and M provide a better idea of the presence and strength of intermolecular interactions between G, M, and the surrounding molecules. For both monoterpenes, the apparent size when they are diluted in organic solvent was considerably lower, especially when dissolved in chloroform, due to the absence of hydrogen bond with the solvent. In DMSO-d_6 they could form a hydrogen bond with the solvent, justifying the slight increase in the apparent hydrodynamic radius. The apparent hydrodynamic radius for both ES components in both solvents was very

Table 5
Properties of phase change of the GM ESs. Glass transition (T_g), melting (T_m), and crystallization (T_{cr}) temperatures. Melting (ΔH_m), and crystallization (ΔH_{cr}) enthalpies.

ESs	T_g/ K	T_m/ K	ΔH_m/ (kJ/mol)	T_{cr}/ K	ΔH_{cr}/ (kJ/mol)
GM12	243.91	278.57	2.0196	253.61	1.1514
GM11	246.40	258.69	0.3083	241.77	0.2288
GM21	–	–	–	–	–

Table 6
Summary of the thermophysical properties [a] of the GM ESs at 101.3 kPa and at two T.

Property	T/ K	GM12	GM11	GM21
Density, ρ/(kg/m^3)	298.15	890.34	890.07	884.67
	313.15	879.30	879.10	873.69
Speed of sound, u/(m/s)	298.15	1382.03	1391.01	1401.16
	313.15	1329.59	1338.63	1348.76
Refractive index, n_D	298.15	1.46513	1.46777	1.47019
	313.15	1.45894	1.46146	1.46379
Isobaric molar heat capacity, $C_{p,m}$/(J/mol·K)	298.15	306	342	337
	313.15	326	359	353
Static permittivity, ε_r	298.15	5.199	6.283	6.849
	313.15	4.597	5.647	6.117
Surface tension, γ/(mN/m)	298.15	28.79	28.61	28.53
	313.15	27.62	27.27	27.26
Dynamic viscosity, η/(mPa·s)	298.15	19.16	13.34	10.16
	313.15	8.64	6.74	5.67

[a] Standard uncertainties are: $u(T) = 0.01$ K; $u(p) = 0.5$ kPa. The combined expanded uncertainties (0.95 level of confidence, k = 2) are: $U_c(\rho) = 0.05$ (kg/m^3); $U_c(u) = 0.5$ (m/s); $U_c(C_{p,m}) = 1$ %; $U_c(n_D) = 2.10^{-5}$; $U_c(\varepsilon_r) = 0.02$; $U_c(\gamma) = 1$ %; $U_c(\eta) = 1$ %.

similar, in agreement with their similar size and molecular weight. On the other hand, very little difference was observed across G and the different ES compositions and between G and M, with a slight increase in the apparent size in mixtures rich in M, due to the increase in hydrogen bonds between M molecules, and the pairs G-M. Otherwise, there was no evidence of strong aggregation. Additionally, alongside with the introduction of TMS, we have assessed the uncertainty in the measurement of diffusion coefficient and its dependency to slight changes in the composition. For this purpose, three replicas were prepared for each mixture. The exact composition and diffusion coefficients for all three components (G, M, and TMS) were determined, and the standard deviation and coefficients of variation, $CV(p)$, for the three replicas were calculated as follows:

$$CV(p) \Big/ \% = \left(\frac{\sigma(p)}{\mu(p)}\right) \cdot 100, \qquad \text{(eq. 26a)}$$

being $\sigma(p)$ the standard deviation and $\mu(p)$ the mean for the parameter p (Full data in Table S3). As data show, the error introduced in the sample preparation due to inaccuracy in the components weighting process (up to 4.6 % in GM11), is magnified in the determination of the self-diffusion coefficient (up to 6.2 % in GM11). This fact renders the values not fully reliable for comparison with different batches of ES, and can mislead when compared among compositions due to the strong dependence to temperature and viscosity. However, using TMS as a reference and reporting the ratio D(TMS)/D(i) reduces the error one order of magnitude (below 0.85 % in GM11), rendering the measurements more accurate and robust.

4.2. Phase change

Table 5 lists the values of the properties of phase change obtained in this study. Experimental determination of the full solid-liquid phase diagram of this system was not possible due to the extremely low value of the melting temperature of pure geraniol. The corresponding thermograms are shown in Fig. S10. The glass transition temperature (T_g) of the equimolar mixture was slightly higher than the value for GM12. The rest of the properties, melting temperature (T_m) and enthalpy (ΔH_m), and crystallization temperature (T_{cr}) and enthalpy (ΔH_{cr}) decreased with increasing the mole fraction of G in the eutectic. In fact, no thermal events were detected in the richest-G mixture (Fig. S10c). We already observed this problem in the geraniol:thymol system (Esfahani et al., 2024). It is a consequence of the very low value of the melting point of the pure G, $T_m = 183$ K (Štejfa et al., 2015).

4.3. Thermophysical properties

The investigation primarily focused on examining various thermophysical properties including density (ρ), speed of sound (u), refractive index (n_D), static permittivity (ε_r), isobaric molar heat capacity ($C_{p,m}$), surface tension (γ), and kinematic viscosity (ν). These

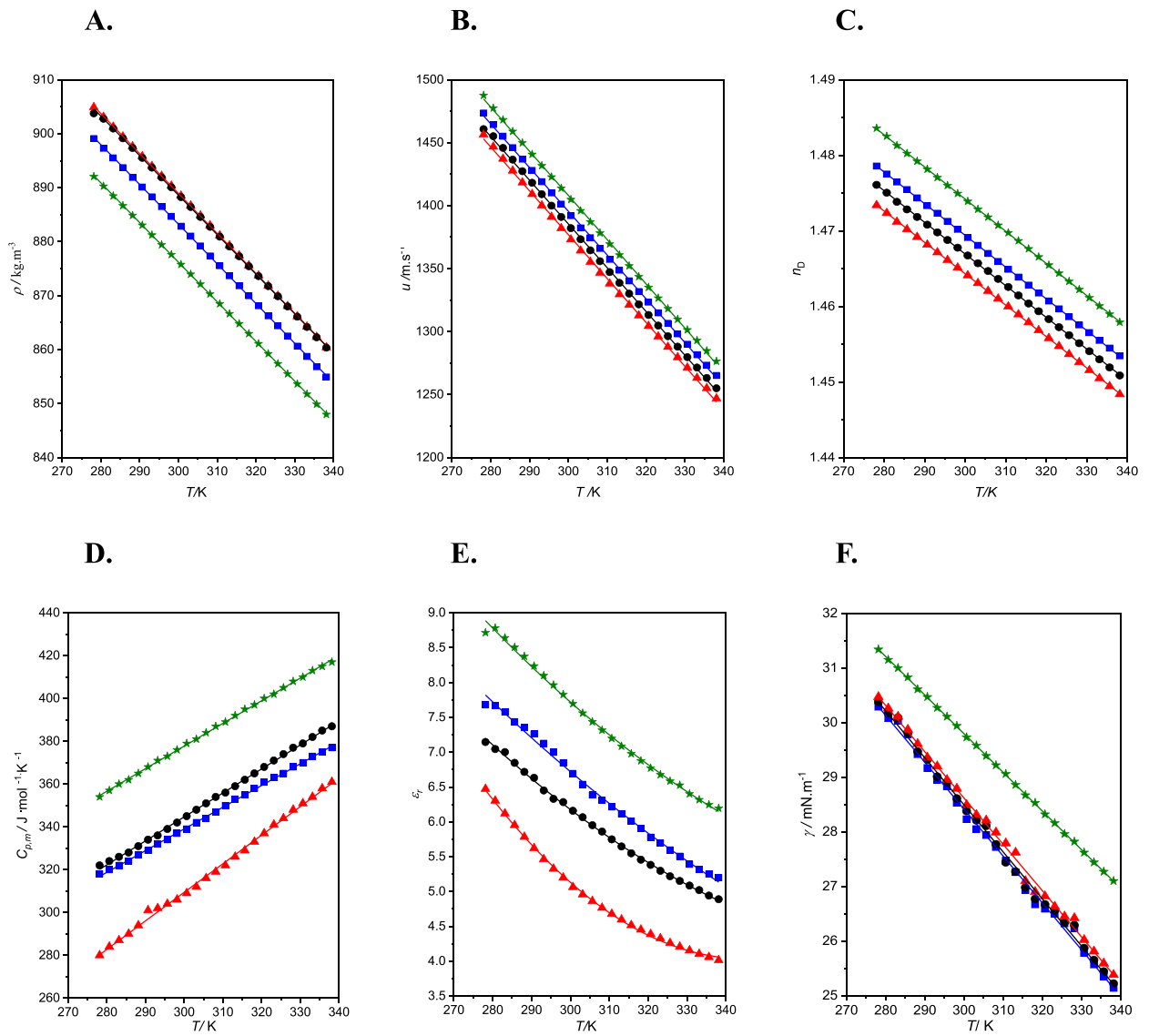

Fig. 5. Experimental properties of the solvents studied at $p = 0.1$ MPa, and at various temperatures (T) and compositions, in molar ratio. **A.** Density (ρ); **B.** Speed of sound (u); **C.** Refraction index (n_D); **D.** Isobaric molar heat capacity ($C_{p,m}$); **E.** Relative static permittivity (ε_r); and **F.** Surface tension (γ). (★), pure geraniol (G) (Esfahani et al., 2024); (▲), geraniol:l-menthol (1:2) (GM12); (●), geraniol:l-menthol (1:1) (GM11); (■), geraniol: l-menthol (2:1) (GM21). Points, experimental values; lines, correlated data.

properties were determined under specific conditions, with a pressure (p) of 0.1 MPa and temperatures ranging from 278.15 to 338.15 K. From ρ and ν data, dynamic viscosity was calculated ($\eta = \rho\nu$) and tabulated. The values of each property at two specific temperatures (T = 298.15 K and 313.15 K) are listed in Table 6. In addition, the experimental data for all temperatures are reported in Table S4 and shown in Fig. 5, and those calculated of different derived properties are listed in Table S5. It is strongly recommended to employ correlations and models that facilitate value prediction in operational conditions in different operational conditions than those used in the experimental characterization. To obtain the values of the properties at different T within the range studied, we used a linear equation for $\rho, u, C_{p,m},$ and $n_D,$ a second-degree polynomial for ε_r, and an exponential correlation for η. Table 7 reports the equations and fitting parameters. For the GM system, no values of these properties were found in the literature but a comparison was made with our previous results (Esfahani et al., 2024) of the pure G and geraniol:thymol system.

4.3.1. Density

The ρ of the studied GM ESs ranged from 854.93 to 904.91 kg m^{-3} and was higher than that of pure G (Esfahani et al., 2024). For GM12 and GM11, the values were indistinguishable and slightly higher (5 kg·m^{-3}) than those of GM21. The slight influence of the composition would be justified by the similarity in the molar volumes (V_m) of both pure components (at 298.15 K, V_m (G) = 175.75 mL·

Table 7
Fitting parameters (A_Y, B_Y, C_Y) and regression coefficients, R^2, for the thermophysical properties of the GM ESs studied.

Property	ESs	A_Y	B_Y	C_Y	R^2
Density [a], ρ/(kg/m^3)	GM12	1111.05	−0.7405		0.99993
	GM11	1108.14	−0.7318		0.99976
	GM21	1103.74	−0.7354		0.99992
Speed of sound [a], u/(m/s)	GM12	2420.87	−3.4798		0.99936
	GM11	2427.13	−3.4723		0.99967
	GM21	2436.66	−3.4706		0.99966
Refractive index [a], n_D	GM12	1.58889	$-4.1 \cdot 10^{-4}$		0.99993
	GM11	1.59260	$-4.2 \cdot 10^{-4}$		0.99992
	GM21	1.59530	$-4.2 \cdot 10^{-4}$		0.99999
Isobaric molar heat capacity [a], $C_{p,m}$/(J/mol·K)	GM12	91.08	1.33508		0.99744
	GM11	80.38	1.12092		0.99910
	GM21	34.62	1.01477		0.99920
Static permittivity [b], ε_r	GM12	68.557	−0.3741	$5.42 \cdot 10^{-4}$	0.99905
	GM11	37.612	−0.1674	$2.09 \cdot 10^{-4}$	0.99835
	GM21	34.019	−0.1349	$1.46 \cdot 10^{-4}$	0.99639
Surface tension [a], γ/(mN/m)	GM12	54.06	−0.0848		0.99740
	GM11	54.35	−0.0862		0.99683
	GM21	54.18	−0.0859		0.99651
Dynamic viscosity [c], η/(mPa·s)	GM12	0.01921	797.10	182.67	0.99999
	GM11	0.01442	938.74	160.83	0.99996
	GM21	0.00583	1316.67	121.91	0.99975

[a] $Y = A_Y + B_Y T$; [b] $Y = A_Y + B_Y T + C_Y T^2$; [c] $Y = A_Y \exp\left[\frac{B_Y}{T - C_Y}\right]$.

mol^{-1}, and V_m (M) = 175.58 mL·mol^{-1}) and the ideality of the mixtures shown in section 4.1. For processes involving phase separation, a difference between the densities of the solvents higher than 5 % is essential (Rodríguez-Llorente et al., 2020). According to this, our mixtures would be suitable for phase separation processes because this difference was of 11 %. The ρ values of GM system were lower than those found for the GT. The differences decreased as the proportion of G in the mixture (x_G) increased. Specifically, they were 48, 30, and 21 kg·m^{-3} at 298.15 K. This discrepancy could be attributed to the less planar structure of M versus T due to the absence of an aromatic ring in the structure of the former. In industry, it is very useful to have tools for calculating properties whose values are crucial in the design of processes. Density is one of the most important. Here, PC-SAFT EoS (section 3.1) was validated for GM system using the VLXE software (Laursen, 2012). Walker et al. (2022) have published an open-source version containing this EoS, among others. The value of the average relative mean deviation between the experimental density values and those predicted by this EoS ($k_{ij} = 0$) was 0.35 %. By optimizing a binary interaction parameter ($k_{ij} = -0.02$), this deviation dropped to 0.11 %. Table S6 and Fig. S11A show the deviations for each composition. Fig. 5A illustrates the relationship between ρ and T in the mixtures under study. It shows that the density decreased as T or x_G increased, consistent with a weakening of the intermolecular interactions.

The design of industrial operations considers the impact of T on ρ a basic parameter to know due to the possibility of fluctuations of T in facilities, which can significantly influence the processes. This is assessed by calculating the isobaric thermal expansion coefficient (α_p) as follows:

$$\alpha_p = -\frac{1}{\rho}\left(\frac{\partial \rho}{\partial T}\right)_p, \quad \text{(eq. 27)}$$

The differences of the values of α_p of the GM mixtures (Table S5) were within the estimated uncertainty range, so a single average value for all mixtures in the working T range can be given, α_p = 0.83 (±0.04) k·K^{-1}. As expected, this property increased with increasing T due to thermal agitation (Fig. 6A).

4.3.2. Speed of sound

The u values were higher at higher x_G and lower T. They ranged from 1246.87 at 338.15 K for GM12 to 1473.57 m · s^{-1} at 278.15 K for GM21 (Fig. 5B). The coefficients of the linear equation are listed in Table 7. Considering that sound travels faster in more compact compounds, it can be concluded that a decrease in the proportion of cyclic compound favors the decrease in free volume in the fluid. This conclusion can be also made by calculating the isentropic compressibility (κ_S) and later, the free intermolecular length (L_f). The equations are:

$$\kappa_S = \frac{1}{\rho u^2} \quad \text{(eq. 28)}$$

$$L_f = K\sqrt{\kappa_S} \quad \text{(eq. 29)}$$

Where K =(91.368 + 0.3565T)10^{-8} is the constant of Jacobson (2004). The κ_S and L_f data are reported in Table S5 and were from 512.22 to 747.58 (±0.25) TPa^{-1} and from 0.431 to 0.579 (±0.005) Å, respectively. The lower value was obtained for GM21 at 278.15

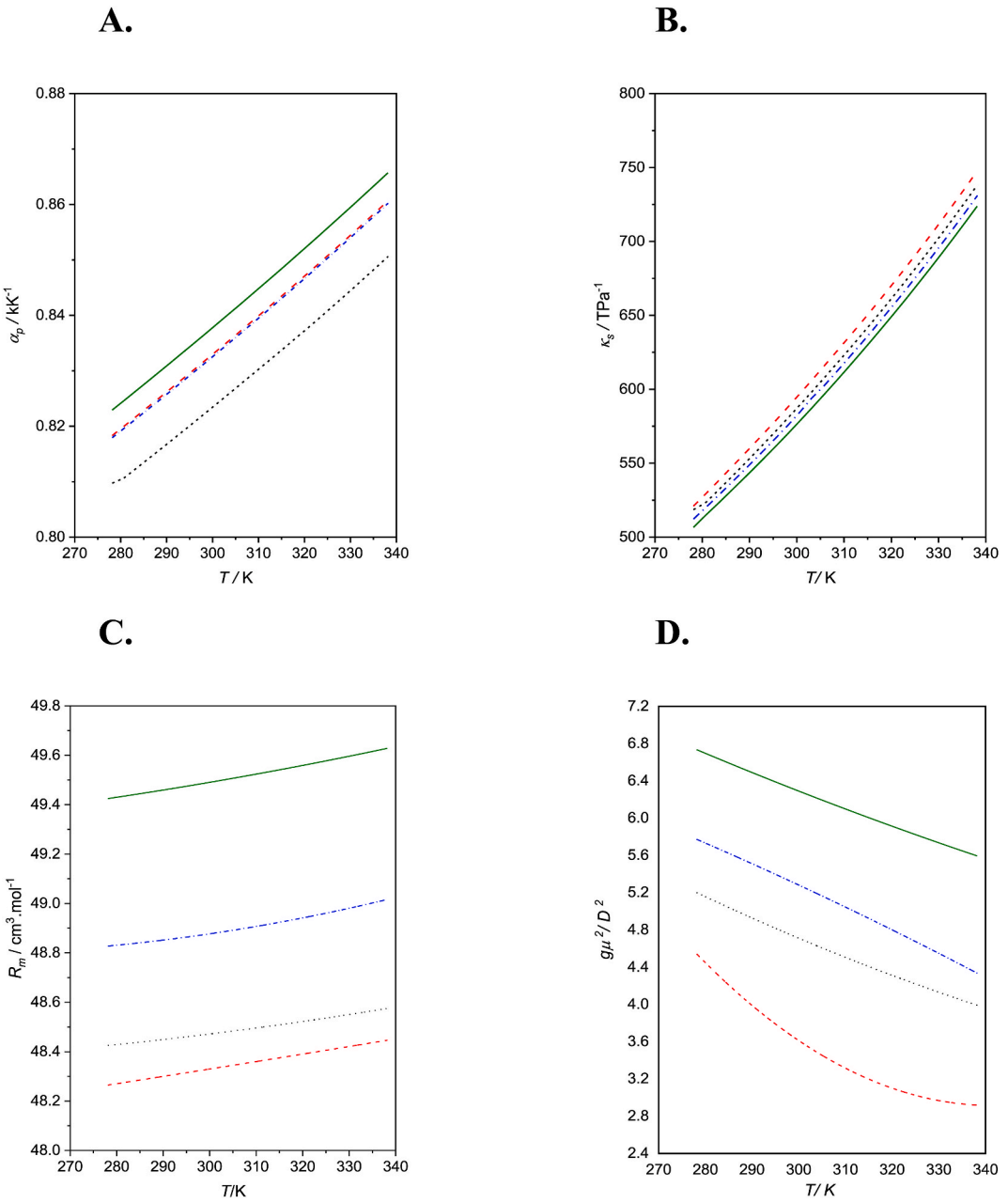

Fig. 6. Calculated properties of the solvents studied at $p = 0.1$ MPa, and at various temperatures (T), and compositions, in molar ratio. **A.** Isobaric thermal expansion coefficient (α_P); **B.** Isentropic compressibility (κ_s); **C.** Molar refraction (R_m); and **D.** Orientational dipolar parameter ($g\mu^2$). (—), pure geraniol (G) (Esfahani et al., 2024); (—·—) geraniol:l-menthol (1:2) (GM12); (· ·) geraniol:l-menthol (1:1) (GM11); (– · –), geraniol:l-menthol (2:1) (GM21).

K, and the higher was found for GM12 at 338.15. Again, the higher the G ratio, the more compact the liquid. Nevertheless, the values showed small differences at similar T. Fig. 6B shows the increase of κ_S with T with similar slope for all compositions. Comparing with the results previously obtained for systems G and geraniol:thymol (GT) mixture, the compaction sequence was: GT > GM ≈ G. Regarding the prediction of u with EoS, it is known that they do not offer good results because this property is calculated from a second derivative. In this work, the average deviations obtained with PC-SAFT were 19 % in all mixtures (Table S6).

4.3.3. Refractive index

The ratio between the values of the speed of light in vacuum and that in the fluid is defined as the refractive index. Therefore, n_D is also related to the volumetric properties of the fluid. The greater the compaction, the greater n_D. The trends observed for GM eutectic

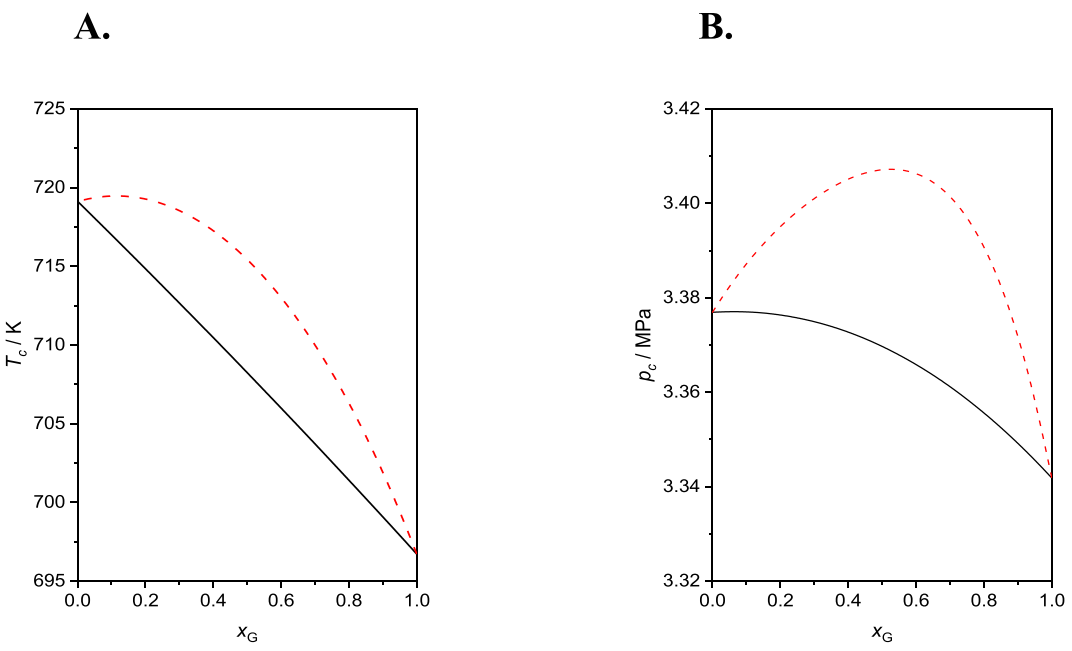

Fig. 7. Critical locus of the geraniol:l-menthol (GM) system estimated with PC-SAFT EoS at two binary interaction parameter (k_{ij}). **A.** Critical temperature (T_c); **B.** Critical pressure (p_c). (—), $k_{ij} = 0$; (**– -**), $k_{ij} = -0.02$.

mixtures were in agreement with the above conclusions. The values increased with x_G and linearity decreased with T (Fig. 5C–Table 7). By comparison, the n_D of GM ESs were lower than those of the pure G and GT ESs. The molar refraction (R_m), is a property indicative of the volume occupied by a mole of hard cores of the molecules and can be calculated with the Lorentz-Lorentz relationship from n_D and ρ at similar conditions (Brocos et al., 2003):

$$R_m = \frac{M}{\rho}\frac{(n_D^2 - 1)}{(n_D^2 + 2)}, \qquad \text{(eq. 30)}$$

Where M is the molar mass (section 2.2). Therefore, an estimate of the free volume (f_m) in the liquid can be made by subtracting the V_m and R_m. This result provides useful insight into the structural information of fluids. The values of R_m and f_m are summarized in Table S5. They ranged from 48.27 to 49.02 (±0.04) $cm^3 \cdot mol^{-1}$, and 123.33 to 132.19 (±0.03) $cm^3 \cdot mol^{-1}$, respectively, increasing with T and x_M (Fig. 6C). From V_m and f_m data, the percentage of free volume at 298.15 K was of 72.3 %, 72.2 %, and 72.1 % for GM12, GM11, and GM21 mixtures. They were higher than those of the GT ESs. This change is due to the absence of the aromatic ring in M which provoked a less compact structure.

4.3.4. Isobaric molar heat capacity

Knowing the heat storage capacity ($C_{p,m}$) of a fluid at various temperatures is basic when considering its application as a phase change material. The obtained values of GM ESs were in the range of 280 $J \cdot mol^{-1} \cdot K^{-1}$ to 387 $J \cdot mol^{-1} \cdot K^{-1}$. They were lower than those of the pure G and increased with T owing to there is more energy in the system capable of being absorbed (Fig. 5D). The linearity of this relationship was lower in the M-rich mixture (Table 7). In the modelling, this property was well predicted by PC-SAFT. The average deviation was of $MRD(C_{p,m}) = 4.3$ and barely varied when introducing an optimized k_{ij} (Table S6, Fig. S11B). The Taherzadeh correlation allows to estimate $C_{p,m}$ from data of the molar mass, critical properties, and acentric factor (section 3.2). These values are similar for G and M, so the calculated data for the three compositions showed hardly any differences. The deviations between our experimental values and those estimated were 5.65 % for GM12 mixture, and exceeded 10 % for the other two.

4.3.5. Static permittivity

The experimental ε_r data offer valuable insights into the polarity and structural analysis of nonionic fluids. The values were within of 7.679 to 4.014. They increased by increasing x_G and decreasing T (Fig. 5E–Table 7). The orientational dipole parameter ($g\mu^2$) can be calculated from $\varepsilon_r, n_D,$ and ρ data with the Fröhlich equation (Fröhlich, 1948):

$$g\mu^2 = \frac{9kT\varepsilon_0 V_m}{N_A}\frac{(\varepsilon_r - n_D^2)(2\varepsilon_r + n_D^2)}{\varepsilon_r (n_D^2 + 2)^2}, \qquad \text{(eq. 31)}$$

where g represents the Kirkwood-Fröhlich correlation parameter, k is the Boltzmann constant, T is the temperature in Kelvin, ε_0 is the

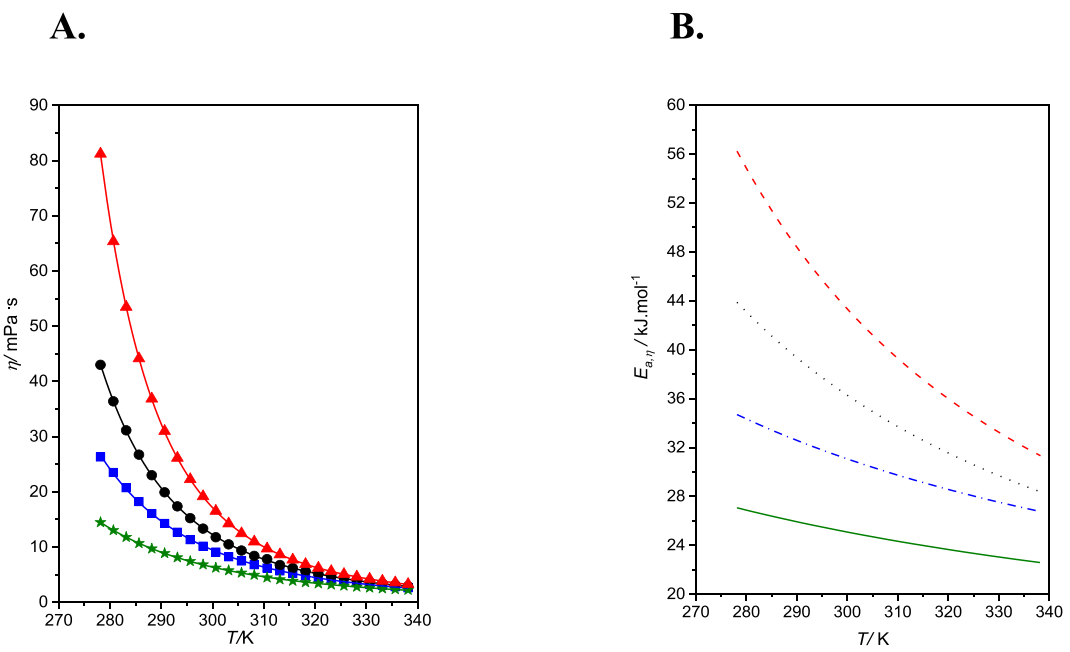

Fig. 8. Transport properties of the solvents studied at $p = 0.1$ MPa, and at various temperatures (T) and compositions, in molar ratio. **A.** Dynamic viscosity (η); **B.** Activation energy for viscous flow ($E_{a,\eta}$) (★). and (—), pure geraniol (G) (Esfahani et al., 2024); (▲) and (—), geraniol:l-menthol (1:2) (GM12); (●) and (· ·), geraniol:l-menthol (1:1) (GM11) (■); and (– · –), geraniol:l-menthol (2:1) (GM21). Points, experimental values; lines, correlated data.

static permittivity in vacuum and N_A, V_m, ε_r, n_D, and μ refer to the Avogadro number, molar volume, relative static permittivity, refractive index, and dipole moment of the fluid at a temperature of T, respectively. The values of this parameter at each temperature are reported in Table S5. They decreased with increasing T (Fig. 6D) and ranged from 2.89 to 5.69 D^2 being lower than those of the pure G. The higher the x_G, the higher the value of the $g\mu^2$. The g factor is an indicator of the relative alignment of adjacent dipoles within a liquid (Bouteloup and Mathieu, 2019). For $g > 1$, the dipoles exhibit a preferential parallel arrangement. For $g < 1$, the fluid has mostly antiparallel dipoles. Lacking experimental data, the dipole moment of a mixture can be estimated as $\mu^2 = \sum_i x_i \mu_i^2$, where μ_i and x_i are the dipole moment and mole fraction of each pure component. Using the μ_i values found in the literature (Schmitz et al., 2015; Strzemski et al., 2022) the g parameter of our mixtures ranged from 0.96 to 1.61. These values were lower than those of the pure G and GT ESs.

4.3.6. Surface tension

Surface tension is the property that characterizes the liquid-air interface. It is strongly related to the droplet formation capability so its value can condition the efficiency of processes in which atomization is required (Lund et al., 1993). The investigated GM ESs presented similar values and were within the range of 25.14–30.47 mN/m. The T_c is an essential property used in both equations of state and thermodynamic models. However, its experimental measurement is often impossible, especially for temperature-sensitive compounds. Considering that the PC-SAFT EoS (section 3.1) has been validated for these mixtures (section 4.2.1), we have used it to obtain the critical properties of the GM system. The critical properties of mixtures can be also calculated from the values of the pure compounds using the Lee-Kesler mixing rules (section 3.2). In addition, different equations based in the theory of corresponding states as those published by Guggenheim and Eötvos (section 3.3) allow to estimate this property from the γ data. All results are listed in Table S7 and the critical locus is displayed in Fig. 7. The differences between the T_c estimated by the different equations were less than 4 %, with the largest differences being those calculated using the Guggenheim equation. Regarding p_c, the data estimated with the LK rules were 1 MPa lower than those of PC-SAFT. Furthermore, the movement of a molecule from the bulk to the surface of the fluid changes its polarity. Therefore, a relationship between γ and n_D can be proposed (section 3.4). The fit parameters are found in Table S8 and the regression coefficient was greater than 0.996 in all mixtures.

Increasing T makes it difficult for molecules to be arranged in an orderly manner in the liquid so γ decreased as T increased (Fig. 5F–Table 7). The entropy (ΔS_s) and enthalpy (ΔH_S) of the surface per unit area were calculated from the γ-T relationship:

$$\Delta S_s = -\left(\frac{\partial \gamma}{\partial T}\right)_p, \qquad \text{(eq. 32)}$$

$$\Delta H_S = \gamma - T\left(\frac{\partial \gamma}{\partial T}\right)_p, \qquad \text{(eq. 33)}$$

Table 8
The experimental solubility [a] at 298.15 K in water, in GM ESs, and in pure G, of the solutes studied: nitrofurantoin (NF), furosemide (F), quercetin (Q), tetracycline (TC), and carvedilol (CVD). It is expressed as $(W_i \pm \sigma_i)^b$ and mole fraction $(x_i)^c$.

	Solute				
Solvent	W_{NF} /x_{NF}	W_F /x_F	W_Q /x_Q	W_{TC} /x_{TC}	W_{CVD} /x_{CVD}
Water	$(8.1 \pm 0.4)\cdot10^{-5}$ [d] /$6.12\cdot10^{-6}$	$7.66\cdot10^{-5}$ [e] /$4.17\cdot10^{-6}$	$(4.3 \pm 0.2)\cdot10^{-7}$ [d] /$2.56\cdot10^{-8}$	$(7.6 \pm 0.6)\cdot10^{-4}$ [d] /$3.08\cdot10^{-5}$	$(1.73 \pm 0.23)\cdot10^{-5}$ [f] /$7.66\cdot10^{-7}$
GM12	$(6.82 \pm 0.4)\cdot10^{-5}$ /$4.46\cdot10^{-5}$	$(1.85 \pm 0.09)\cdot10^{-3}$ /$8.70\cdot10^{-4}$	0.016 ± 0.001 /$8.17\cdot10^{-3}$	0.015 ± 0.001 /$5.22\cdot10^{-3}$	0.021 ± 0.001 /$7.97\cdot10^{-3}$
GM11	$(8.33 \pm 0.24)\cdot10^{-5}$ /$5.43\cdot10^{-5}$	$(2.18 \pm 0.12)\cdot10^{-3}$ /$1.02\cdot10^{-3}$	0.019 ± 0.001 /$9.67\cdot10^{-3}$	0.018 ± 0.001 /$6.25\cdot10^{-3}$	0.028 ± 0.001 /$1.06\cdot10^{-2}$
GM21	$(1.97 \pm 0.13)\cdot10^{-4}$ /$1.28\cdot10^{-4}$	$(2.76 \pm 0.07)\cdot10^{-3}$ /$11.29\cdot10^{-3}$	0.024 ± 0.001 /$1.22\cdot10^{-2}$	0.020 ± 0.001 /$6.92\cdot10^{-3}$	0.030 ± 0.002 /$1.13\cdot10^{-2}$
G	$(3.57 \pm 0.13)\cdot10^{-4}$ /$2.31\cdot10^{-4}$	$(3.63 \pm 0.10)\cdot10^{-3}$ /$1.69\cdot10^{-3}$	0.028 ± 0.002 /$1.41\cdot10^{-2}$	0.026 ± 0.001 /$8.94\cdot10^{-3}$	0.042 ± 0.001 /$1.57\cdot10^{-2}$

[a] The uncertainties are: $u(W_{NF}) = 3.3\cdot10^{-6}$, $u(W_F) = 1.6\cdot10^{-5}$, $u(W_Q) = 3.6\cdot10^{-6}$, $u(W_{TC}) = 6.2\cdot10^{-6}$, $u(W_{CVD}) = 1.6\cdot10^{-5}$; [b] $W_i = g_i / g_{solvent}$; $\sigma_i = \sqrt{\frac{\sum (W_i - \overline{W_i})^2}{N}}$; [c] $x_i = n_i / (n_i + n_{solvent})$; [d] Ref. (Bergua et al., 2021a); [e] Ref. (Shin and Kim, 2003); [f] Ref (Lomba et al., 2024).

The mixtures had similar behavior with T so an average value of these properties can be given. They were 0.085 ± 0.009 mN·m^{-1}·K^{-1}, and 54.2 ± 0.1 mN·m^{-1}, respectively.

4.3.7. Viscosity

The fluidity of the solvents is an essential property in the design and optimization of industrial processes. Factors as molecular size, shape, and intermolecular interactions influence in its value. In this section, we present the results of the dynamic viscosity (η) of the GM mixtures studied. The higher the M ratio, the more viscous the mixture was. The values were lower than the value of 100 mPa s proposed as the upper limit for ensuring optimal performance in engineering processes (Van Osch et al., 2019). They ranged from 81.22 to 2.61 mPa·s. The effect of the T on the transport properties is very pronounced, especially at lower T. Therefore, an exponential relation between them is usually found (Fig. 8A). Here, we used the VFT equation (Garca-Coln et al., 1989) whose parameters are listed in Table 7. The first parameter (A_Y) represents the viscosity at infinite temperature, indicating that fluidity at that point is solely governed by steric constraints. The remaining coefficients (B_Y and C_Y) lead us to calculate the energetic barrier of a molecule for penetrating between the layers of the fluid. For instance, the energy of viscosity flow of solvents ($E_{a,\eta}$):

$$E_{a,\eta} = R\frac{\partial(\ln \eta)}{\partial\left(\frac{1}{T}\right)} = R\left(\frac{B_Y}{\left(\frac{C_Y^2}{T^2} - \frac{2C_Y}{T} + 1\right)}\right), \quad \text{(eq. 34)}$$

The $E_{a,\eta}$ calculated values are collected in Table S5 and displayed in Fig. 8B.

Considering the sequences found for A_Y and $E_{a,\eta}$, we can conclude that increasing the M ratio increased both the steric hindrance and the strength of the intermolecular interactions. These results were aligned with those thermodynamic properties previously discussed. In addition, our mixtures had η and $E_{a,\eta}$ values higher than those of the mixtures with T. This fact could be linked with the less compactness of the system studied here due to the absence of aromatic ring in M structure. Both η and γ are related to the structure into the bulk of the fluid, so correlations between these properties can be applied. We used the Pelofsky and Murkerjee (section 3.4) equations and the coefficients are reported in Table S8. In both correlations, the logarithmic fit presented good linearity but those of Murkerjee was better ($R^2 > 0.97$).

4.4. Solubility study

The solubility is quantified as the concentration of the solute which dissolves in a saturated solution at a given temperature. This concept is related to the ability of the solute and the solvent to interact spontaneously to give rise to a homogeneous molecular dispersion. Solute and solvent would be at equilibrium in the saturated solution. The solubility of a solute in a solvent depends on the characteristics of the solute, the properties of the solvent, and different parameters of the solubilization process. Solutes with non-planar structures form fewer stable crystals, which therefore break more easily and consequently have higher solubilities (Ishikawa and Hashimoto, 2011). The ability of the solute to form hydrogen bonds is given by the sum of the number of hydrogen bond acceptors (HBAs) and donors (HBDs). This total number and the topological polar surface area (TPSA) allow us to evaluate the polarity of the solute. Solvents with a higher percentage of free volume have a greater capacity to interact with the solute and therefore, to dissolve it. In addition, low-viscosity solvents facilitate the diffusion of the solute within the liquid. Among operational factors, an adequate agitation as well as an increase in temperature weakens the cohesive forces facilitating solute-solvent interaction. In systems with hydrophobic eutectic solvents, the prevailing hypothesis suggests that the improvement of the solubility of APIs is due to both the

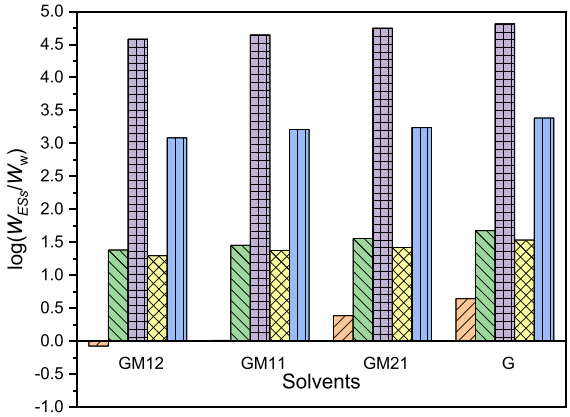

Fig. 9. Logarithmic ratio between the solubility of several APIs in the studied solvents (W_{ESs}) and in water (W_w). APIs: nitrofurantoin; furosemide; quercetin; tetracycline, and carvedilol. Solvents: (GM12), geraniol:l-menthol (1:2); (GM11), geraniol:l-menthol (1:1); (GM21), geraniol:l-menthol (2:1); (G), pure geraniol.

formation of hydrogen bonds as the hydrophobic interactions (Devi et al., 2023; Padilla et al., 2024).

We evaluated the solubility, in terms of grams of solute per grams of solvent ($W_i = g_i/g_{solvent}$), of five poorly water-soluble APIs both in the pure G and GM ESs. The APIs chosen were nitrofurantoin (NF), furosemide (F), quercetin (Q), tetracycline (TC), and carvedilol (CVD). According to the biopharmaceutical classification system (BCS), they belong to different classes depending on their solubility in water and permeability. The NF, Q, and CVD belong to class II (low solubility and high permeability), TC is classified as class III substance (high solubility and low permeability), and F is a class IV (low solubility and permeability) substance (Pharmacopeia of the United States of America, 32nd revision, and the National Formulary, 27th edition, 2009). The experimental results of this work and those of aqueous solubility found in the literature are given in Table 8. The table also includes the standard deviation obtained in the statistical analysis. In water, the solubility ratio between the most soluble API (TC) and the least soluble (Q) was 1750 times. This fact is unexpected considering that Q is the second API, behind TC, with the highest TPSA, HBAs, and HBDs. Nevertheless, Q is a planar molecule, so its crystalline form has a high lattice energy. In addition, it does not have sp^3 carbons ($Fsp^3 = 0$) so the capacity to occupy target space is low. On the other hand, TC has the highest value of Fsp^3. It has been shown that designing drugs with a higher value of this factor is a valid strategy for improving aqueous solubility (Wei et al., 2020). Table S9 lists the values of these structural properties for all studied APIs. The solubility of NF in GM12 was slightly lower than in water. However, it was higher in the other solvents, increasing with increasing G ratio. On the other hand, the solubility of F, Q, TC, and CVD was higher in all ESs than in water (Fig. 9). This result was especially remarkable for Q and CVD with a ratio (W_{ESs}/W_w) of $6.5{\cdot}10^4$ and $2.5{\cdot}10^3$, respectively. The ranking of solubility in the ESs studied was CVD > Q ≈ TC > F > NF. This sequence is practically the same as that found for their molar refractivity (proportional to polarizability) and very different from that corresponding to polarity. Considering the lipophilicity value of TC (Table S9), its solubility in our hydrophobic solvents might surprise. However, it is also a very polarizable molecule with a great hydrophobic area. All of the above indicated that, although both the APIs and G and M possess the ability to form hydrogen bonds, the dominant interactions are those of van der Waals established between their hydrophobic regions. The importance of this type of interaction in hESs was already observed in the solubilization of lidocaine in camphor-based mixtures (Padilla et al., 2024). A trend of solubility with composition of GM ESs was found. The higher x_G, the higher the solubility value, and pure G showed the highest affinity for APIs. This could be related to a greater ease of interaction with the free chain of G compared to M, the former having a greater number of rotatable bonds. In addition, the lower viscosity of the solvent as x_G increases facilitated its contact with the solute.

The literature reports solubility data (Table S10) for NF, Q, and TC with the hydrophobic binary mixtures of thymol, l-menthol, and octanoic or decanoic acids (Bergua et al., 2021a, 2022a, 2022b). Furthermore, the solubility of Q with different hydrophilic mixtures was published (Bergua et al., 2021b; López et al., 2020; Oliveira et al., 2020; Rodríguez-Juan et al., 2021). For F and CVD, solubility data were only found with hydrophilic eutectic solvents (Lomba et al., 2023a, 2023b, 2024; Sayad et al., 2021). The W_{NF} values in this study were higher than those published for the mixtures of l-menthol with carboxylic acids but lower than the data for the mixtures of l-menthol and thymol (Fig. 10A). The W_Q in this work was much higher than that published for most mixtures. Only two hydrophilic aqueous mixtures of glucose or xylitol and choline chloride presented similar values (Fig. 10C). The TC was less soluble in the GM ESs and in pure G than in the other hydrophobic mixtures. (Fig. 10D). Finally, both F and CVD were markedly more soluble in our hydrophobic mixtures than in the majority of the hydrophilic ones studied (Fig. 10B and E). Therefore, our geraniol-based mixtures would be better solvent alternatives for F, Q, and CVD. For NF and TC, a comparison of the bioactive properties of the specific components of each ES would be necessary.

5. Conclusion

A study of the structure and the thermophysical behaviour of hydrophobic eutectic mixtures composed of l-menthol and geraniol (GM ESs) in varying molar ratios (1:2, 1:1, and 2:1) was performed. Several techniques of nuclear magnetic resonance were used to

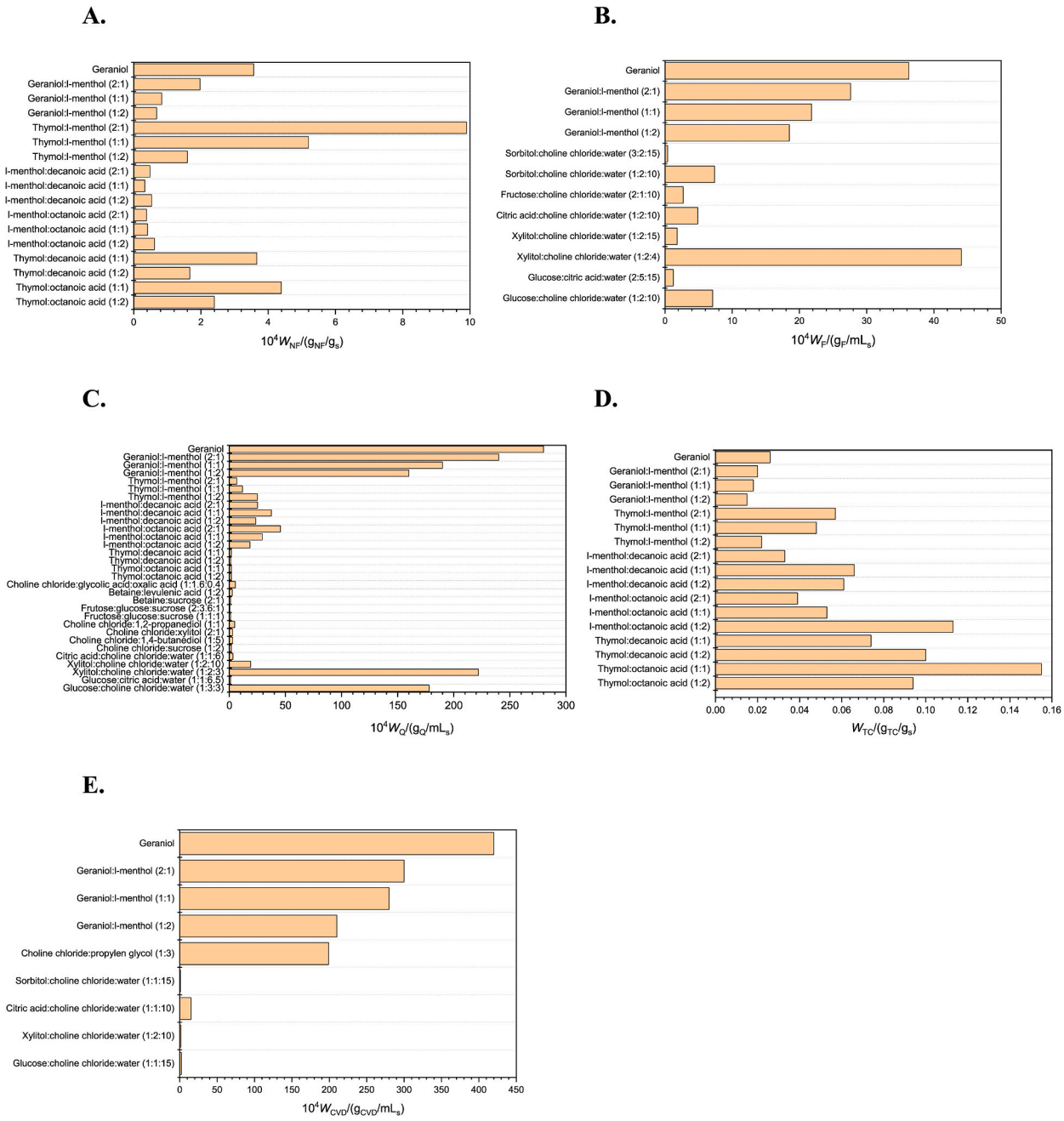

Fig. 10. Comparison between our solubility data and those from literature for the APIs studied in different eutectic mixtures. **A.** nitrofurantoin; **B.** furosemide; **C.** quercetin; **D.** tetracycline; and **E.** carvedilol.

elucidate the molecular structure and compute the auto-diffusion coefficients and apparent size of the compounds in the mixtures. Thermodynamic and transport properties as density, speed of sound, refractive index, isobaric molar heat capacity, static permittivity, surface tension, and dynamic viscosity were measured and discussed. At the final stage, the aforementioned liquids were utilized to evaluate the solubility of five poorly-water soluble active pharmaceutical ingredients namely nitrofurantoin, furosemide, quercetin, tetracycline and carvedilol. The results were analyzed taking into account the structural properties of the solutes and the thermophysical ones of the solvents.

From the NMR experiments, we can conclude that the GM ESs behaved as ideal mixtures. Additionally, the use of TMS as an inert reference in the determination of the diffusion coefficients provided more accurate and reliable data, enabling the estimation of apparent hydrodynamic radius that can be compared among different mixtures and solutions. The thermophysical characterization indicated that the solvents studied could be suitable for industrial applications involving separation of organic and aqueous phases.

The density of the liquids was about 110 kg/m^3 lower than that of water, and the values of the surface tension and dynamic viscosity were moderate. Furthermore, we observed a preferred parallel orientation of the dipoles that was favored at higher concentration of geraniol. From the solubility experiments carried out, it is concluded that the eutectic mixtures were better solvents than water, with the highest values being found with pure geraniol. In general, a trend of the solubility with the polarity and the symmetry of the solute was observed in the aqueous solution. The trend was observed with the molar refractivity in the hydrophobic solvents.

CRediT authorship contribution statement

Mohammadreza Haftbaradaran Esfahani: Resources, Methodology, Formal analysis, Data curation. **Fernando Bergua:** Formal analysis, Data curation. **Ignacio Delso:** Writing – original draft, Validation, Investigation. **Carlos Lafuente:** Supervision, Project administration, Investigation. **Manuela Artal:** Writing – review & editing, Writing – original draft, Supervision, Conceptualization.

Declaration of competing interest

The authors declare that they have no known competing financial interests or personal relationships that could have appeared to influence the work reported in this paper.

Acknowledgments

PLATON research group acknowledges financial support from Gobierno de Aragón and Fondo Social Europeo “Construyendo Europa desde Aragón” _E31_23R. Fernando Bergua is thankful for the financial assistance (INVESTIGO-020-22) granted by the Ministerio de Ciencia e Innovación (Spain) (MICIU/AEI/10.13039/501100011033), “Unión Europea NextGeneration EU/PRTR”.

Appendix A. Supplementary data

Supplementary data to this article can be found online at https://doi.org/10.1016/j.scp.2025.102070.

Data availability

The authors confirm that the data supporting the findings of this study are available within the article and its supplementary materials

References

Abdelquader, M.M., Li, S., Andrews, G.P., Jones, D.S., 2023. Therapeutic deep eutectic solvents: a comprehensive review of their thermodynamics, microstructure and drug delivery applications. Eur. J. Pharm. Biopharm. 186, 85–104. https://doi.org/10.1016/j.ejpb.2023.03.002.

Antón, V., Artigas, H., Muñoz-Embid, J., Artal, M., Lafuente, C., 2017. Thermophysical study of 2-acetylthiophene: experimental and modelled results. Fluid Phase Equilib. 433, 126–134. https://doi.org/10.1016/j.fluid.2016.10.026.

Baka, E., 2010. Development and Examination of Solubility Measurement Methods for Drug Solubility Determination. Smmelweis University, Budapest.

Becker, J., Manske, C., Randl, S., 2022. Green chemistry and sustainability metrics in the pharmaceutical manufacturing sector. Curr Opin Green Sustain Chem 33, 100562. https://doi.org/10.1016/j.cogsc.2021.100562.

Bergua, F., Castro, M., Lafuente, C., Artal, M., 2022a. Thymol+l-menthol eutectic mixtures: thermophysical properties and possible applications as decontaminants. J. Mol. Liq. 368, 120789. https://doi.org/10.1016/j.molliq.2022.120789.

Bergua, F., Castro, M., Muñoz-Embid, J., Lafuente, C., Artal, M., 2022b. L-menthol-based eutectic solvents: characterization and application in the removal of drugs from water. J. Mol. Liq. 352, 118754. https://doi.org/10.1016/j.molliq.2022.118754.

Bergua, F., Castro, M., Muñoz-Embid, J., Lafuente, C., Artal, M., 2021a. Hydrophobic eutectic solvents: thermophysical study and application in removal of pharmaceutical products from water. Chemical Engineering Journal 411. https://doi.org/10.1016/j.cej.2021.128472.

Bergua, F., Delso, I., Muñoz-Embid, J., Lafuente, C., Artal, M., 2021b. Structure and properties of two glucose-based deep eutectic systems. Food Chem. 336, 127717. https://doi.org/10.1016/j.foodchem.2020.127717.

Bouteloup, R., Mathieu, D., 2019. Predicting dielectric constants of pure liquids: fragment-based Kirkwood-Fröhlich model applicable over a wide range of polarity. Phys. Chem. Chem. Phys. 21, 11043–11057. https://doi.org/10.1039/c9cp01704f.

Brocos, P., Piñeiro, Á., Bravo, R., Amigo, A., 2003. Refractive indices, molar volumes and molar refractions of binary liquid mixtures: concepts and correlations. Phys. Chem. Chem. Phys. 5, 550–557. https://doi.org/10.1039/B208765K.

Cabrita, E.J., Berger, S., 2001. DOSY studies of hydrogen bond association: tetramethylsilane as a reference compound for diffusion studies. Magn. Reson. Chem. 39, S142–S148. https://doi.org/10.1002/mrc.917.

Chen, W., Viljoen, A.M., 2010. Geraniol - a review of a commercially important fragrance material. South Afr. J. Bot. 76, 643–651. https://doi.org/10.1016/j.sajb.2010.05.008.

de Castro Teixeira, A.P., de Sousa Melo, F.M., Lima, I.O., de Luna Freire Pessôa, H., de Cássia da Silveira e Sá, R., 2024. Do menthol and its derivatives present biological activity with antifungal potential? J. Essent. Oil Res. 36, 291–320. https://doi.org/10.1080/10412905.2024.2376673.

Delso, I., Lafuente, C., Muñoz-Embid, J., Artal, M., 2019. NMR study of choline chloride-based deep eutectic solvents. J. Mol. Liq. 290, 111236. https://doi.org/10.1016/j.molliq.2019.111236.

Devi, M., Moral, R., Thakuria, S., Mitra, A., Paul, S., 2023. Hydrophobic deep eutectic solvents as greener substitutes for conventional extraction media: examples and techniques. ACS Omega 8, 9702–9728. https://doi.org/10.1021/acsomega.2c07684.

Esfahani, M.H., Bergua, F., Delso, I., Lafuente, C., Artal, M., 2024. Geraniol and hydrophobic geraniol:thymol eutectic mixtures: structure and thermophysical characterization. Ind. Crops Prod. 222, 119781. https://doi.org/10.1016/j.indcrop.2024.119781.

Fröhlich, H., 1948. General theory of the static dielectric constant. Trans. Faraday Soc. 44, 238–243. https://doi.org/10.1039/TF9484400238.

Ganorkar, S.B., Hadole, P.M., Patil, M.R., Pardeshi, C.V., Bobade, P.S., Shirkhedkar, A.A., Vander Heyden, Y., 2025. Deep eutectic solvents in analysis, delivery and chemistry of pharmaceuticals. Int J Pharm 672, 125278. https://doi.org/10.1016/j.ijpharm.2025.125278.
Garca-Coln, L.S., del Castillo, L.F., Goldstein, P., 1989. Theoretical basis for the Vogel-Fulcher-Tammann equation. Phys. Rev. B 40, 7040–7044. https://doi.org/10.1103/PhysRevB.40.7040.
Gross, J., Sadowski, G., 2002. Application of the perturbed-chain SAFT equation of state to associating systems. Ind. Eng. Chem. Res. 41, 5510–5515. https://doi.org/10.1021/ie010954d.
Gross, J., Sadowski, G., 2001. Perturbed-chain SAFT: an equation of state based on a perturbation theory for chain molecules. Ind. Eng. Chem. Res. 40, 1244–1260. https://doi.org/10.1021/ie0003887.
Guggenheim, E.A., 1945. The principle of corresponding states. J. Phys. Chem. 13, 253–261.
Harten, P., Martin, T., Gonzalez, M., Young, D., 2020. The software tool to find greener solvent replacements, PARIS III. Environ. Prog. Sustain. Energy 39, 1–7. https://doi.org/10.1002/ep.13331.
Hernández-Serrano, V., Muñoz-Embid, J., Bergua, F., Lafuente, C., Artal, M., 2023. pVT behaviour of hydrophilic and hydrophobic eutectic solvents. J. Mol. Liq. 382. https://doi.org/10.1016/j.molliq.2023.122019.
Hokkala, E., Strachan, C.J., Agopov, M., Järvinen, E., Semjonov, K., Heinämäki, J., Yliruusi, J., Svanbäck, S., 2024. Thermodynamic solubility measurement without chemical analysis. Int J Pharm 653, 123890. https://doi.org/10.1016/j.ijpharm.2024.123890.
Ishikawa, M., Hashimoto, Y., 2011. Improvement in aqueous solubility in small molecule drug discovery programs by disruption of molecular planarity and symmetry. J. Med. Chem. 54, 1539–1554. https://doi.org/10.1021/jm101356p.
Jacobson, B., 2004. Ultrasonic velocity in liquids and liquid mixtures. J. Chem. Phys. 20, 927–928. https://doi.org/10.1063/1.1700615.
Katrak, V.K., Patel, N.A., Ijardar, S.P., 2025. The physicochemical properties and plausible implication of deep eutectic solvents in analytical techniques. Crit. Rev. Anal. Chem. 1–24. https://doi.org/10.1080/10408347.2025.2486209.
Könczöl, Á., Dargó, G., 2018. Brief overview of solubility methods: recent trends in equilibrium solubility measurement and predictive models. Drug Discov. Today Technol. 27, 3–10. https://doi.org/10.1016/j.ddtec.2018.06.001.
Laursen, T., 2012. VLXE ApS.
Lee, B.I., Kesler, M.G., 1975. A generalized thermodynamic correlation based on three-parameter corresponding states. AIChE J. 21, 510–527. https://doi.org/10.1002/aic.690210313.
Li, H., Yang, K., Yang, Y., Ding, L., Li, X., 2025. Natural deep eutectic solvents (NADES) in drug delivery systems: characteristics, applications, and future perspectives. Int J Pharm 675, 125509. https://doi.org/10.1016/j.ijpharm.2025.125509.
Lomba, L., Polo, A., Alejandre, J., Martínez, N., Giner, B., 2023a. Solubility enhancement of caffeine and furosemide using deep eutectic solvents formed by choline chloride and xylitol, citric acid, sorbitol or glucose. J. Drug Deliv. Sci. Technol. 79, 104010. https://doi.org/10.1016/j.jddst.2022.104010.
Lomba, L., Polo, A., Martínez, N., Alejandre, J., Giner, B., 2024. Solubility and stability of carvedilol in deep eutectic solvents: a step towards a sustainable pharmaceutical formulation in the liquid state. ChemistrySelect 9. https://doi.org/10.1002/slct.202305218.
Lomba, L., Polo, A., Werner, Á., Lafuente, C., Giner, B., 2023b. Deep eutectic solvents based on sugars for oral applications. Eur. J. Pharm. Biopharm. 191, 103–113. https://doi.org/10.1016/j.ejpb.2023.08.007.
López, N., Delso, I., Matute, D., Lafuente, C., Artal, M., 2020. Characterization of xylitol or citric acid:choline chloride:water mixtures: structure, thermophysical properties, and quercetin solubility. Food Chem. 306. https://doi.org/10.1016/j.foodchem.2019.125610.
Lund, M.T., Sojka, P.E., Lefebvre, A.H., Gosselin, P.G., 1993. Effervescent atomization at low mass flow rates. Part I: the influence of surface tension. Atomization Sprays 3, 77–89. https://doi.org/10.1615/AtomizSpr.v3.i1.40.
Ma, S., Cai, C., Lu, Q., Tan, Z., 2025. A review of green solvents for the extraction and separation of bioactive ingredients from natural products. Food Chem. 478, 143703. https://doi.org/10.1016/j.foodchem.2025.143703.
Maczka, W., Winska, K., Grabarczyk, M., 2020. One hundred faces of geraniol. Molecules (Basel). https://doi.org/10.3390/molecules25143303.
Martín, M.I., García-Díaz, I., Rodríguez, M.L., Gutiérrez, M.C., del Monte, F., López, F.A., 2024. Synthesis and properties of hydrophilic and hydrophobic deep eutectic solvents via heating-stirring and ultrasound. Molecules (Basel) 29, 3089. https://doi.org/10.3390/molecules29133089.
Martins, M.A.R., Crespo, E.A., Pontes, P.V.A., Silva, L.P., Bülow, M., Maximo, G.J., Batista, E.A.C., Held, C., Pinho, S.P., Coutinho, J.A.P., 2018. Tunable hydrophobic eutectic solvents based on terpenes and monocarboxylic acids. ACS Sustain Chem Eng 6, 8836–8846. https://doi.org/10.1021/acssuschemeng.8b01203.
Molero-Sangüesa, M., Jiménez-Omeñaca, I., Bergua, F., Artigas, H., Lafuente, C., Artal, M., 2024. Thermophysical properties of lidocaine:thymol or L-menthol eutectic mixtures. J. Taiwan Inst. Chem. Eng. 163. https://doi.org/10.1016/j.jtice.2024.105631.
Mulet, A., Carcel, J., Benedito, J., Rosselló, C., Simal, S., 2016. Ultrasonic mass transfer enhancement in Food processing. In: Transport Phenomena in Food Processing. CRC Press, Boca Raton, Florida, USA, pp. 287–300.
Mushtaq, M., Butt, F.W., Akram, S., Ashraf, R., Ahmed, D., 2024. Deep eutectic liquids as tailorable extraction solvents: a review of opportunities and challenges. Crit. Rev. Anal. Chem. 54, 1634–1660. https://doi.org/10.1080/10408347.2022.2125284.
Oliveira, G., Wojeicchowski, J.P., Farias, F.O., Igarashi-Mafra, L., de Pelegrini Soares, R., Mafra, M.R., 2020. Enhancement of biomolecules solubility in aqueous media using designer solvents as additives: an experimental and COSMO-based models' approach. J. Mol. Liq. 318, 114266. https://doi.org/10.1016/j.molliq.2020.114266.
Oyoun, F., Toncheva, A., Henríquez, L.C., Grougnet, R., Laoutid, F., Mignet, N., Alhareth, K., Corvis, Y., 2023. Deep eutectic solvents: an eco-friendly design for drug engineering. ChemSusChem 16. https://doi.org/10.1002/cssc.202300669.
Padilla, N., Delso, I., Bergua, F., Lafuente, C., Artal, M., 2024. Characterization of camphor: thymol or dl-menthol eutectic mixtures; Structure, thermophysical properties, and lidocaine solubility. J. Mol. Liq. 405. https://doi.org/10.1016/j.molliq.2024.125069.
Papazian, H.A., 1971. Correlation of surface tension between various liquids. J. Am. Chem. Soc. 93, 5634–5636. https://doi.org/10.1021/ja00751a008.
Pelofsky, A.H., 1966. Surface tension-viscosity relation for liquids. J. Chem. Eng. Data 11, 394–397. https://doi.org/10.1021/je60030a031.
Quintana, A.A., Sztapka, A.M., Santos Ebinuma, V. de C., Agatemor, C., 2022. Enabling sustainable chemistry with ionic liquids and deep eutectic solvents: a fad or the future? Angew. Chem. Int. Ed. 61. https://doi.org/10.1002/anie.202205609.
Rodríguez-Juan, E., López, S., Abia, R., G, J., Muriana, F., Fernández-Bolaños, J., García-Borrego, A., 2021. Antimicrobial activity on phytopathogenic bacteria and yeast, cytotoxicity and solubilizing capacity of deep eutectic solvents. J. Mol. Liq. 337, 116343. https://doi.org/10.1016/j.molliq.2021.116343.
Rodríguez-Llorente, D., Cañada-Barcala, A., Muñoz, C., Pascual-Muñoz, G., Navarro, P., Santiago, R., Águeda, V.I., Álvarez-Torrellas, S., García, J., Larriba, M., 2020. Separation of phenols from aqueous streams using terpenoids and hydrophobic eutectic solvents. Sep. Purif. Technol. 251, 117379. https://doi.org/10.1016/j.seppur.2020.117379.
Sayad, T., Poturcu, K., Moradi, M., Rahimpour, E., Zhao, H., Jouyban, A., 2021. Solubility study of carvedilol in the aqueous mixtures of a choline chloride/propylene glycol deep eutectic solvent. J. Mol. Liq. 342, 117537. https://doi.org/10.1016/j.molliq.2021.117537.
Schmitz, D., Shubert, V.A., Betz, T., Schnell, M., 2015. Exploring the conformational landscape of menthol, menthone, and isomenthone: a microwave study. Front. Chem. 3. https://doi.org/10.3389/fchem.2015.00015.
Shaibuna, M., Theresa, L.V., Sreekumar, K., 2022. Neoteric deep eutectic solvents: history, recent developments, and catalytic applications. Soft Matter 18, 2695–2721. https://doi.org/10.1039/D1SM01797G.
Shereshefsky, J.L.L., 1930. Surface tension of saturated vapors and the equation of Eötvos. J. Phys. Chem. 35, 1712–1720. https://doi.org/10.1021/j150324a014.
Shin, S.-C., Kim, J., 2003. Physicochemical characterization of solid dispersion of furosemide with TPGS. Int J Pharm 251, 79–84. https://doi.org/10.1016/S0378-5173(02)00586-0.
Sil, A., Sangeeta, Bhati, R., Das, S., Guchhait, B., 2023. Ion clustering, aggregation and diffusion in amide based deep eutectic solvents: a microstructural investigation using various NMR spectroscopic techniques and molecular dynamics simulation. J. Mol. Liq. 388, 122761. https://doi.org/10.1016/j.molliq.2023.122761.
Štejfa, V., Dergal, F., Mokbel, I., Fulem, M., Jose, J., Růžička, K., 2015. Vapor pressures and thermophysical properties of selected monoterpenoids. Fluid Phase Equilib. 406, 124–133. https://doi.org/10.1016/j.fluid.2015.07.031.

Strzemski, M., Dresler, S., Podkościelna, B., Skic, K., Sowa, I., Załuski, D., Verpoorte, R., Zielińska, S., Krawczyk, P., Wójciak, M., 2022. Effectiveness of volatile natural deep eutectic solvents (VNADESs) for the green extraction of chelidonium majus isoquinoline alkaloids. Molecules (Basel) 27, 2815. https://doi.org/10.3390/molecules27092815.

Taherzadeh, M., Haghbakhsh, R., Duarte, A.R.C., Raeissi, S., 2020. Estimation of the heat capacities of deep eutectic solvents. J. Mol. Liq. 307, 112940. https://doi.org/10.1016/j.molliq.2020.112940.

Van Osch, D.J.G.P., Dietz, C.H.J.T., Van Spronsen, J., Kroon, M.C., Gallucci, F., Van Sint Annaland, M., Tuinier, R., 2019. A search for natural hydrophobic deep eutectic solvents based on natural components. ACS Sustain Chem Eng 7, 2933–2942. https://doi.org/10.1021/acssuschemeng.8b03520.

Virk, A.S., Torres, A.M., Willis, S.A., Price, W.S., 2016. NMR diffusion studies of spherical molecules: tetramethylsilane and buckyballs. J. Mol. Liq. 214, 157–161. https://doi.org/10.1016/j.molliq.2015.11.029.

Walker, P.J., Yew, H.-W., Riedemann, A., 2022. Clapeyron.jl: an extensible, open-source fluid thermodynamics toolkit. Ind. Eng. Chem. Res. 61, 7130–7153. https://doi.org/10.1021/acs.iecr.2c00326.

Wei, W., Cherukupalli, S., Jing, L., Liu, X., Zhan, P., 2020. Fsp3: a new parameter for drug-likeness. Drug Discov. Today 25, 1839–1845. https://doi.org/10.1016/j.drudis.2020.07.017.

Zheng, X., Yin, F., Gong, G., Zhang, X., He, S., Tang, W., Wei, X.-H., 2025. An overview of hydrophobic deep eutectic solvents driven liquid-phase extraction: applications and prospects. J. Chromatogr. A 1748, 465824. https://doi.org/10.1016/j.chroma.2025.465824.

Zielińska-Błajet, M., Pietrusiak, P., Feder-Kubis, J., 2021. Selected monocyclic monoterpenes and their derivatives as effective anticancer therapeutic agents. Int. J. Mol. Sci. 22, 4763. https://doi.org/10.3390/ijms22094763.

Zimmerman, J.B., Anastas, P.T., Erythropel, H.C., Leitner, W., 2020. Designing for a green chemistry future. Science (1979) 367, 397–400. https://doi.org/10.1126/science.aay3060.